

The short-term association between environmental variables and mortality: evidence from Europe

Jens Robben^{1,2,3,4,5,*}, Katrien Antonio^{1,2,3,4,5}, and Torsten Kleinow^{2,5}

¹*Faculty of Economics and Business, KU Leuven, Belgium.*

²*Faculty of Economics and Business, University of Amsterdam, The Netherlands.*

³*LRisk, Leuven Research Center on Insurance and Financial Risk Analysis, KU Leuven, Belgium.*

⁴*LStat, Leuven Statistics Research Center, KU Leuven, Belgium.*

⁵*RCLR, Research Centre for Longevity Risk, University of Amsterdam, The Netherlands.*

* Corresponding author: jens.robben@kuleuven.be

Version: August 21, 2024

Abstract

Using fine-grained, publicly available data, this paper studies the short-term association between environmental factors, i.e., weather and air pollution characteristics, and weekly mortality rates in small geographical regions in Europe. Hereto, we develop a mortality modeling framework where a baseline model describes a region-specific, seasonal trend observed within the historical weekly mortality rates. Using a machine learning algorithm, we then explain deviations from this baseline using features constructed from environmental data to identify anomalies and extreme events. We illustrate our proposed modeling framework through a case study on more than 550 NUTS 3 regions (Nomenclature of Territorial Units for Statistics, level 3) in 20 European countries. Using interpretation tools, we unravel insights into which environmental features are most important when estimating excess or deficit mortality relative to the baseline and explore how these features interact. Moreover, we investigate harvesting effects through our constructed weekly mortality modelling framework. Our findings show that temperature-related features are most influential in explaining mortality deviations from the baseline over short time periods. Furthermore, we find that environmental features prove particularly beneficial in southern regions for explaining elevated levels of mortality, and we observe evidence for a harvesting effect related to heat waves.

Keywords: weekly mortality modeling; high-resolution gridded datasets; environmental data

1 Introduction

The relevance of environmental factors in assessing mortality risk spans several sectors including health care, urban planning, and life insurance. In the epidemiological and medical literature, studies have consistently unveiled short-term associations between temperature and mortality statistics. For instance, both heat waves and cold spells can cause immediate increases in mortality, possibly with a delay of a few days or weeks ([Basu & Samet, 2002](#)). Extreme weather events such as heavy rainfall, extreme drought, or wind storms also play a crucial role on mortality in the short term ([Weilnhammer et al., 2021](#)). Furthermore, epidemiological evidence underscores the adverse health effects of air pollution ([Brunekreef & Holgate, 2002](#); [Rückerl](#)

et al., 2011). Specifically, Orellano et al. (2020) find positive short-term associations between air pollution, including particulate matter, nitrogen dioxide, and ozone, and daily mortality outcomes. The focal point of studies investigating short-term associations differs from long-term studies that examine the impact of chronic or prolonged exposure to air pollution on mortality. Such studies typically use cohort-based methods, where researchers track a group of participants over time, and consider the air pollution levels in the areas where they reside (Bentayeb et al., 2015; Hoek et al., 2013). In this paper, we aim to identify and analyze the primary environmental factors associated with mortality deviations from a region-specific baseline mortality model, which describes the overall seasonal trend observed in the historical mortality rates of a given region and age group. Our focus is on short-term associations, particularly at a weekly and regional level within Europe.

The proposed framework for weekly mortality modeling comprises two building blocks. The first building block is the region-specific baseline mortality model. To construct this baseline, we design a Serfling-type mortality model, incorporating sine and cosine Fourier terms to capture weekly seasonality (Serfling, 1963). The second building block aims to analyze deviations from the baseline mortality model as a function of short-term effects of region-specific environmental anomalies and extreme environmental indices. Environmental anomalies measure deviations from a time-dependent, baseline level of the environmental factors under consideration, while extreme environmental indices express how often an environmental factor surpasses a specified high quantile or falls below a particular low quantile within a week. This second building block allows to unravel the short-term associations between the observed deviations from the mortality baseline and environmental features capturing events like heat waves, cold spells, or heightened levels of air pollution. Due to the large number of environmental features under consideration and their potential complex interplay, we adopt a machine learning approach to learn and estimate these intricate, non-linear short-term (interaction) effects when modeling mortality rates.

In Europe, the EuroMOMO project has emerged as an initiative for monitoring weekly excess mortality across 28 participating European countries or sub-national regions.¹ EuroMOMO, known as the European network for MOnitoring excess MOrtality, estimates weekly all-cause excess deaths in a standardized manner. EuroMOMO's objective is to support swift detection of excess mortality signals, particularly related to pandemics, influenza, emerging infections, and extreme environmental conditions. Hereto, the Serfling model is used as mortality baseline when measuring excess mortality (Serfling, 1963). This baseline is estimated with a quasi-Poisson regression model on weekly death counts with a log-linear long-term trend on the one hand, and Fourier terms to address the seasonality inherent in the weekly mortality pattern on the other hand. Additionally, Vestergaard et al. (2020) use the EuroMOMO modeling framework to estimate European-wide weekly mortality rates and excess all-cause mortality during the COVID-19 pandemic. Furthermore, Nielsen et al. (2018) introduce the FluMOMO model as an extension of the weekly Serfling-type baseline mortality model which adds influenza activity and extreme temperatures as explanatory variables to the model. Using this model, Nielsen et al. (2019) estimate the weekly all-cause excess and influenza-attributable mortality during the winter season 2017-2018 in Europe.

Various methodologies have been explored in the epidemiological and medical literature to investigate the association between a particular environmental factor and (daily) mortality rates or death counts. Keatinge et al. (2000) investigate heat-related mortality across Europe by analyzing the region-specific temperatures that correspond to the lowest daily death rates. Another strand of research relies on time series regression models, assuming an overdispersed Poisson

¹Website of the EuroMOMO project: <https://www.euromomo.eu/>.

distribution for the daily death counts with either temperature or a particular air pollutant as an explanatory variable, along with other confounding factors (Armstrong, 2006). While earlier studies favoured a linear relationship between daily deaths and the considered environmental factor, recent research suggests non-linear associations (Braga et al., 2002). Schwartz (2000), Braga et al. (2001), and Pattenden et al. (2003) highlight the delayed effects of a particular air pollutant or temperature measure on mortality, necessitating more advanced modeling techniques such as distributed lag models (DLMs). These models, exemplified by Schwartz (2000), accommodate delayed or lagged effects, crucial in understanding daily mortality patterns following extreme weather events or air pollution spikes. These have been further extended to Distributed Lag Non-linear Models (DLNMs), offering greater flexibility in capturing non-linear effects across both predictor space and lag dimensions (Gasparrini et al., 2010). For a more detailed and technical overview of these methodologies, we refer to Appendix A.

In the actuarial and economic literature, the impact of environmental factors on mortality remains largely underexplored. However, its importance is underscored by the European Insurance and Occupational Pensions Authority (EIOPA) which highlights the need to integrate climate change scenarios into insurers' own risk and solvency assessments (EIOPA, 2021). This need is amplified by the more frequent, intense, and prolonged heat waves that are expected to occur in the 21st century (Meehl & Tebaldi, 2004). Among the scant economic literature, Carleton et al. (2022) find that extreme temperatures, both hot and cold, significantly increase mortality rates, particularly among the elderly, with higher incomes and adaptation reducing some of these effects. Within the actuarial field, there is a substantial body of literature dedicated to modeling mortality rates, particularly focusing on one-year mortality rates and their evolution across time and age. This literature encompasses a variety of approaches tailored to single and multiple populations (Booth & Tickle, 2008; Enchev et al., 2017), potentially integrating socio-economic characteristics (Cairns et al., 2019; Villegas & Haberman, 2014; Wen et al., 2023), but studies regarding the impact of environmental factors on mortality remain rather limited. Li and Tang (2022) delve into the modeling of joint extremes in monthly temperature and death counts using a bivariate peaks-over-threshold approach. Through an empirical study with monthly temperature data and death counts in the United States, they reveal that joint extremes in cold weather and old-age death counts demonstrate the strongest level of dependence. Additionally, Dong et al. (2022) quantify the short-term impact of air quality on monthly mortality rates. Their findings indicate that incorporating PM2.5 air pollution levels, i.e., fine particulate matter consisting of particles that are 2.5 microns or less in diameter, enhances the predictive accuracy for explaining deaths in excess of a pre-established expected number of deaths. Dong et al. (2024) explore the financial impacts of climate-related risks on life insurers by constructing stress scenarios that model short-term and long-term climate shocks on synthetic insurance portfolios to assess their effects on claim payments. Lastly, the American Academy of Actuaries, the Casualty Actuarial Society, the Canadian Institute of Actuaries, and the Society of Actuaries developed the Actuaries Climate Index (ACI), a quarterly measure derived from changes in extreme weather events and sea levels, aiming at offering a practical monitoring tool for tracking climate trends (American Academy of Actuaries et al., 2016).

Our paper contributes to the literature in three ways. First, we construct a weekly mortality baseline model that estimates a seasonal mortality pattern observed in the historical mortality rates of a particular region. We enhance the calibration process of this baseline model by employing a quadratic penalty matrix to obtain parameter estimates for the baseline that exhibit smooth variations across adjacent regions. This approach is particularly advantageous for regions with lower population exposure and we demonstrate this in a case study on individuals aged 65 and older, living across more than 550 European NUTS 3 regions. Second, we leverage insights from fine-grained open data acquired via the Copernicus Climate Data Store (CDS) for

weather factors and the Copernicus Atmospheric Monitoring Service (CAMS) for air pollution factors. Particularly, we use the E-OBS daily gridded meteorological data for Europe from the CDS ([CIESIN et. al, 2018](#)) and the European air quality reanalysis from the CAMS ([INERIS et. al, 2022](#)). These datasets offer high temporal and spatial resolutions, providing detailed information on environmental factors across Europe. By detailing how this raw, fine-grained data can be used to create environmental anomalies and extreme environmental indices, defined on a particular geographic region and temporal scale, we offer valuable insights for researchers and practitioners aiming to integrate such data into their mortality modeling framework. Third, we use this large set of pre-engineered environmental anomalies and extreme environmental indices as inputs in a machine learning model to analyze mortality deviations from the baseline level. As such, we extend the FluMOMO mortality modeling methodology ([Nielsen et al., 2018](#)). Due to the machine learning approach, we do not impose any functional form regarding the effect of the covariates on mortality rates, which allows to capture the complex interactions present in the environmental data. This is in contrast to what is typically done in the epidemiological and medical literature where they solely focus on the short-term impact of an individual environmental factor on mortality.

This paper is organized as follows: Section 2 provides an overview of the notations and data used in this paper. In Section 3, we detail our mortality modeling framework. Specifically, Section 3.1 introduces a weekly, region-specific mortality baseline model, while Section 3.2 details our approach to explain mortality deviations from this baseline using environmental features by means of a machine learning technique. We outline the calibration strategy for both the weekly baseline mortality model and the machine learning model in Section 4. To illustrate the practical application of our methodology, we conduct a case study in Section 5 on the age group 65+, applying our proposed framework to the NUTS 3 regions of 20 European countries. Section 5.1 details the feature engineering process to create environmental anomalies and extreme environmental indices on a weekly time scale and NUTS 3 geographical level, from the raw, fine-grained data. In Section 5.2, we discuss the calibration results of our weekly mortality modeling framework applied to our case study, while Section 5.3 provides further insights and applications. Section 6 concludes and summarizes the key findings of our study.

2 Notations and data

2.1 Notations

Let $d_{x,t,w}^{(r)}$ be the observed death count in region r at age group x during ISO week w of ISO year t .² We denote the set of age groups or buckets under consideration as \mathcal{X} , the range of ISO years as \mathcal{T} and the set of ISO weeks in ISO year t as \mathcal{W}_t . Particularly, the number of ISO weeks in ISO year t is 52 or 53.³ Furthermore, we encode each region by an integer, i.e., we denote the set of regions as $\mathcal{R} = \{1, 2, \dots, R\}$. For the sake of brevity in notation, we omit explicit reference to gender, although the methodologies described in this paper apply to male, female, and unisex data. Moreover, we denote $E_{x,t,w}^{(r)}$ for the exposure-to-risk in region $r \in \mathcal{R}$ at age group $x \in \mathcal{X}$ during ISO week $w \in \mathcal{W}_t$ of ISO year $t \in \mathcal{T}$.

The region-specific weekly force of mortality, denoted by $\mu_{x,t,w}^{(r)}$, represents the instantaneous rate of mortality in region r at age group x and in ISO week w of ISO year t . We define the

²We follow the ISO 8601 standard maintained by the International Organization for Standardization, see <https://www.iso.org/standard/70907.html>.

³A year t consists of 53 ISO weeks if January 1st of that year falls on a Thursday, or if it is a leap year with January 1st being a Wednesday.

observed weekly death rate, i.e., $m_{x,t,w}^{(r)}$, as:

$$m_{x,t,w}^{(r)} = \frac{d_{x,t,w}^{(r)}}{E_{x,t,w}^{(r)}}.$$

Furthermore, $q_{x,t,w}^{(r)}$ refers to the mortality rate and represents the probability that an individual from region r and age group x and who is alive at the start of ISO week w in ISO year t , will die within the next week. Under the assumption that the force of mortality $\mu_{x,t,w}^{(r)}$ is constant within a week, we can estimate the weekly mortality rate as (Pitacco, 2009):

$$q_{x,t,w}^{(r)} \approx 1 - \exp\left(-\mu_{x,t,w}^{(r)}\right), \quad (2.1)$$

for each $x \in \mathcal{X}$, $t \in \mathcal{T}$, $w \in \mathcal{W}_t$ and $r \in \mathcal{R}$.

2.2 Data sources: death counts, exposures and environmental data

Death counts. We extract the deaths by week, sex, 5-year age group and NUTS 3 region throughout the years 2013-2019 from Eurostat for the following 20 European countries:⁴ Austria (AT), Belgium (BE), Switzerland (CH), Czech Republic (CZ), Denmark (DK), Estonia (EE), Spain (ES), Finland (FI), France (FR), Hungary (HU), Italy (IT), Liechtenstein (LI), Lithuania (LT), Luxembourg (LU), Latvia (LV), Norway (NO), Poland (PL), Portugal (PT), Sweden (SE), and Slovakia (SK).⁵ This database uses the ISO-time format for weeks and years. The Nomenclature of Territorial Units for Statistics (NUTS) serves as a geocode standard used to designate the administrative divisions of countries for statistical purposes. The NUTS 3 level is the lowest level in the NUTS classification and corresponds for example to the departments in France (101 regions) and provinces and metropolitan cities in Italy (107 regions). We do not consider the overseas regions in France (Guadeloupe, Martinique, French Guiana, La Réunion, and Mayotte) Portugal (autonomous regions of Madeira and the Azores), Norway (Svalbard and Jan Mayen), and Spain (Canary Islands, Ceuta, and Melilla) in our analysis. Figure 1a visualizes the NUTS 3 regions in the 20 European countries in our study. In the remainder of this paper, we will often use the terms ‘regions’ instead of ‘NUTS 3 regions’ and ‘years’ and ‘weeks’ instead of ‘ISO years’ and ‘ISO weeks’, respectively, for the sake of conciseness.

In this paper, we specifically concentrate on older ages due to their increased vulnerability to the impacts of environmental factors. This approach aligns with previous studies, such as Keatinge et al. (2000) and Sunyer et al. (1996). Hereto, we aggregate the region-specific death counts $d_{x,t,w}^{(r)}$ across the ages 65+, which we denote in the sequel of this paper as $d_{t,w}^{(r)}$ for notational convenience. Figure 1b shows the death counts at age group 65+ across the NUTS 3 regions in the 15th week of the year 2015. We observe three regions with significantly higher observed death counts. These correspond to the three most populated regions across the countries under consideration: Madrid, Barcelona, and Rome. Figure 1c illustrates the weekly death counts spanning the years 2013-2019 across the NUTS 3 regions of Barcelona (ES511), Milano (ITC4C), and Stockholm (SE110). The figure reveals a seasonal trend, with more deaths during winter weeks and relatively lower death counts during the summer weeks.

⁴We begin the time period in 2013 due to the availability of air pollution data, as will be discussed later in this section, and we end it in 2019 to exclude the impact of the COVID-19 pandemic.

⁵Countries such as Germany, the Netherlands, and the United Kingdom are excluded from our analysis due to the unavailability of weekly death counts at the NUTS 3 level for the years 2013-2019. The database can be consulted on https://ec.europa.eu/eurostat/databrowser/view/demo_r_mweek3/default/table?lang=en.

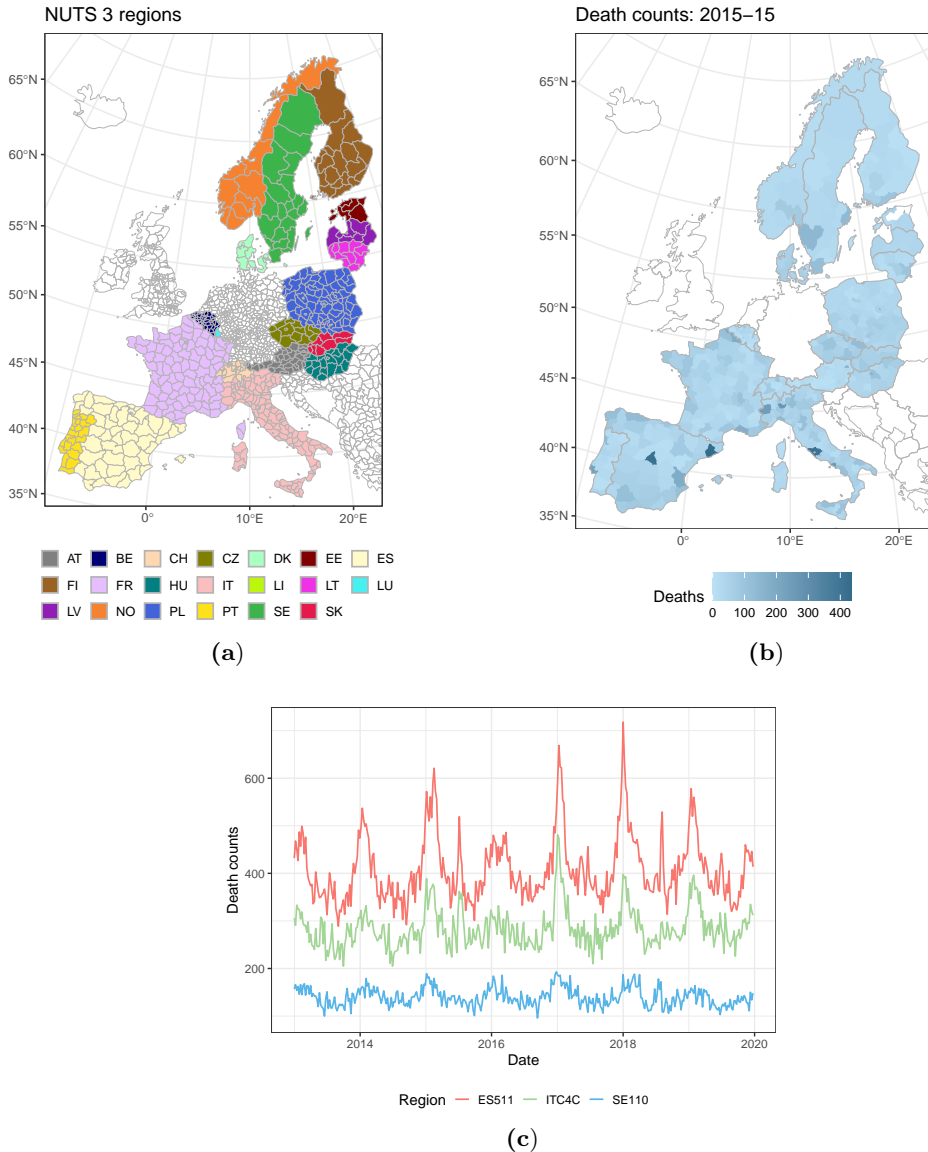


Figure 1: Panel (a) shows the NUTS 3 regions in 20 European countries, excluding overseas regions. Panel (b) illustrates the female death counts in the NUTS 3 regions at the 15-th ISO week of the year 2015. Panel (c) visualizes the weekly female death counts throughout the years 2013-2019 in three NUTS 3 regions in Europe: Barcelona (red), Milano (green), and Stockholm (blue).

Exposure-to-risk. In order to calculate weekly mortality rates, it is necessary to formulate a weekly exposure measure, denoted as $E_{t,w}^{(r)}$, for the age group 65+ in each NUTS 3 region throughout the years 2013-2019. Hereto, we retrieve the population count of people aged 65+ on January 1 of each year t by sex and NUTS 3 region from Eurostat.⁶ We construct an estimate for the weekly exposure similar to the approach proposed in [Jdanov et al. \(2021\)](#), and obtain:

$$E_{t,w}^{(r)} = \frac{P_{t,0}^{(r)} + P_{t+1,0}^{(r)}}{2 \cdot 52.18}, \quad (2.2)$$

⁶The database can be accessed on the web page: https://ec.europa.eu/eurostat/databrowser/view/demo_r_pjanaggr3/default/table?lang=en.

for $t \in \{2013, \dots, 2019\}$, with $P_{t,0}^{(r)}$ the population count of people aged 65+ at January, 1 of year t in region $r \in \mathcal{R}$.⁷ The number 52.18 represents the average number of weeks per year.⁸

Weather data. To retrieve weather factors, we consult the Copernicus Climate Data Store (CDS). The CDS provides access to a wide range of weather-related data, including observations, reanalysis, and projections with different spatial and temporal resolutions.⁹ These datasets have been shown to be a good alternative to weather station data in temperature-mortality assessments across different regions (de Schrijver et al., 2021).

Particularly, we use the E-OBS land-only, gridded meteorological data for Europe from 1950 onwards, derived from in-situ observations, see Copernicus Climate Change Service, Climate Data Store (2020). The E-OBS dataset is constructed using observations gathered by meteorological stations across Europe and provided by the National Meteorological and Hydrological Services (NMHS) and other affiliated institutes. It is a daily, high-resolution gridded dataset, where weather factors are measured on grids with a spatial resolution of 0.10° (≈ 11 km) in both longitude and latitude direction.

Table 1 lists the weather factors that we use in this paper, i.e., we extract the daily maximum temperature T_{max} , the daily average temperature T_{avg} , the daily minimum temperature T_{min} , the daily average relative humidity Hum , the total daily precipitation $Rain$, and the daily average wind speed $Wind$. We opt for these weather factors due to their relevance in epidemiological and medical research, particularly concerning their impact on mortality. For instance, Barnett (2010) finds that the daily minimum, average, and maximum temperatures all have a comparable level of predictive power to explain daily death counts. Findings from studies such as Braga et al. (2002) and Alberdi et al. (1998) did not find a significant impact of humidity and wind speed, respectively, on daily mortality. Nevertheless, we explore these weather factors in our set of considered environmental factors for verification purposes.

Weather factor	Explanation
T_{max}	Daily maximum air temperature, measured in degrees Celsius ($^\circ C$) at 2 meters above surface.
T_{avg}	Daily average air temperature, measured in $^\circ C$ at 2 meters above surface.
T_{min}	Daily minimum air temperature, measured in $^\circ C$ at 2 meters above surface.
Hum	Daily average relative humidity, measured at 2 meters above surface. Relative humidity is defined as the percentage of actual humidity to saturation humidity and falls within the range of [0, 100]. Saturation humidity occurs when the air contains the maximum amount of moisture possible at a specific temperature.
$Rain$	The daily total precipitation expressed in mm , including rain, snow, and hail, and measured as the height of equivalent liquid water per square meter.
$Wind$	Daily average wind speed in m/s , measured at 10 metres above the surface.

Table 1: Weather variables retrieved from the E-OBS gridded meteorological dataset on the CDS.

We extract the E-OBS daily weather factors in Europe across a grid that covers the 20 European countries highlighted in Figure 1a, and spans the years 2013-2019. As an example, Figures 2a

⁷The subscript 0 refers to the start, i.e., January 1, of year t .

⁸While the current approach assumes a constant weekly exposure within a year, a more advanced method could employ linear interpolation for a smoother transition of weekly exposures between consecutive years.

⁹Reanalysis is the process of using climate models to combine observational data with historical climate information to produce comprehensive time series of climate variables on a (sub)daily time scale.

and 2b display, respectively, the daily maximum temperature and the total precipitation amount at two randomly selected dates within the considered time range 2013-2019. Figure 2c illustrates the maximum temperature on August 2 on the 2013-2019 timeline to show the fluctuation in the maximum temperature on that particular day across the historical period under consideration.

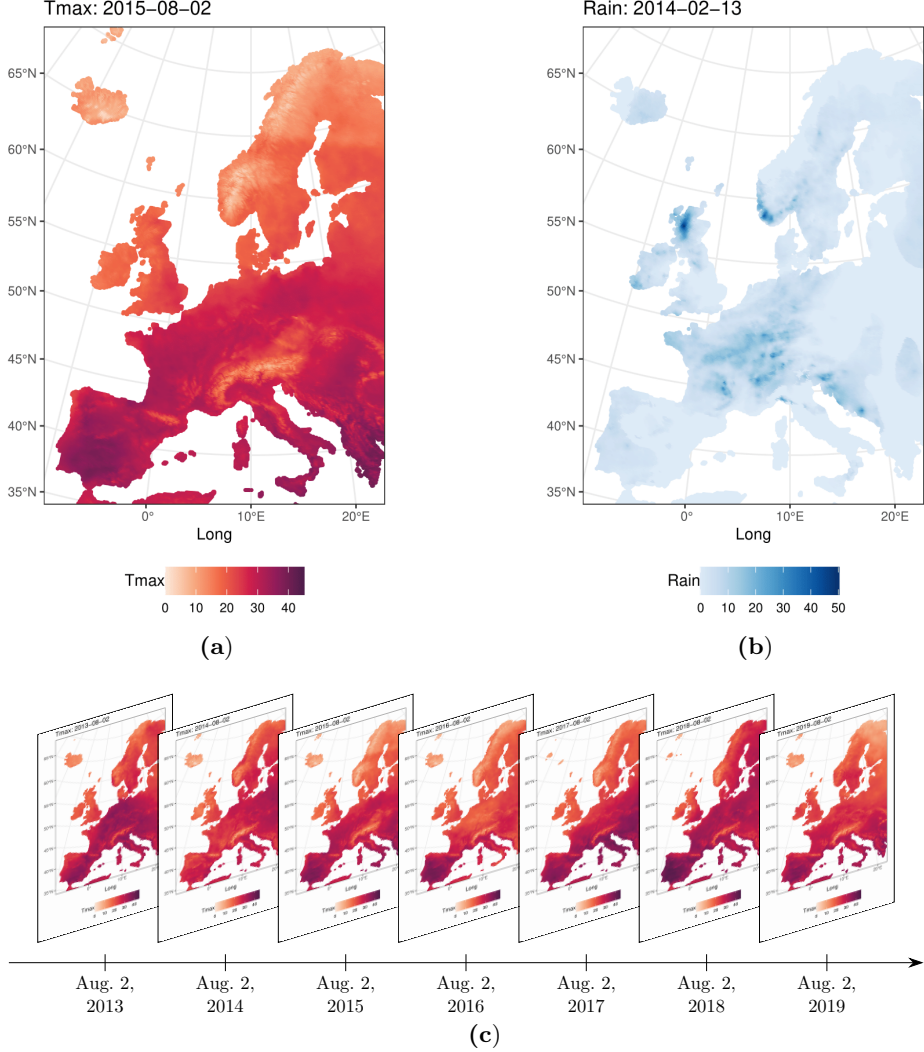


Figure 2: Panel (a) shows the maximum temperature on August 2, 2015, panel (b) the total precipitation amount on February 13, 2014, and panel (c) the maximum temperature on August 2 in the years 2013-2019, in Europe.

Air pollution data. To access air pollution measurements, we consult the Atmosphere Data Store (ADS), a platform that facilitates the implementation of the Copernicus Atmosphere Monitoring Service (CAMS). This monitoring service offers comprehensive, historical, and real-time data on the atmospheric composition, such as air quality, greenhouse gases, and aerosols.

We rely on the CAMS European air quality reanalyses dataset (INERIS et. al, 2022), which delivers hourly air quality reanalyses for Europe based on validated observations for the years 2013-2020. This reanalysis integrates both model data and observations from the European Environment Agency (EEA) using data assimilation techniques, with the inclusion of satellite data to enhance in-situ observations. Similar to the E-OBS data, this air quality dataset is a high-resolution gridded dataset. Measurements of several air pollutants are available on a fine

grid with a spatial resolution of 0.10° (≈ 11 km) in both longitude and latitude directions and a temporal resolution of one hour. Table 2 lists the air pollutants that we will use in this paper, i.e., O₃, N_O₂, PM10, and PM2.5. We select these air pollutants because of their demonstrated significant short-term impact on mortality in the literature. For example, [Pascal et al. \(2014\)](#) identify short-term impacts of PM10 and PM2.5 levels on daily mortality in nine French cities. In addition, [Orellano et al. \(2020\)](#) find short-term impacts of ozone and nitrogen dioxide on daily mortality based on a systematic review including 196 studies.

Air pollutants	Explanation
O ₃	Hourly ozone levels, measured in micrograms per cubic meter ($\mu\text{g}/\text{m}^3$).
N _O ₂	Hourly nitrogen dioxide levels ($\mu\text{g}/\text{m}^3$).
PM10	Hourly particular matter levels of particles with a diameter of 10 microns or less ($\mu\text{g}/\text{m}^3$).
PM2.5	Hourly fine particular matter levels of particles with a diameter of 2.5 microns or less ($\mu\text{g}/\text{m}^3$).

Table 2: Air pollutants retrieved from the CAMS European air quality reanalyses dataset.

We gather hourly CAMS air pollution measurements in Europe for the years 2013-2019 and focus on the air pollutants in Table 2. Unlike the E-OBS dataset, this data covers both land and sea. To illustrate, Figures 3a and 3b present the O₃ and PM10 concentrations, respectively, at two randomly selected times. We highlight the boundaries of the 20 European countries under consideration in red to provide a clear visualization of the land component of interest.

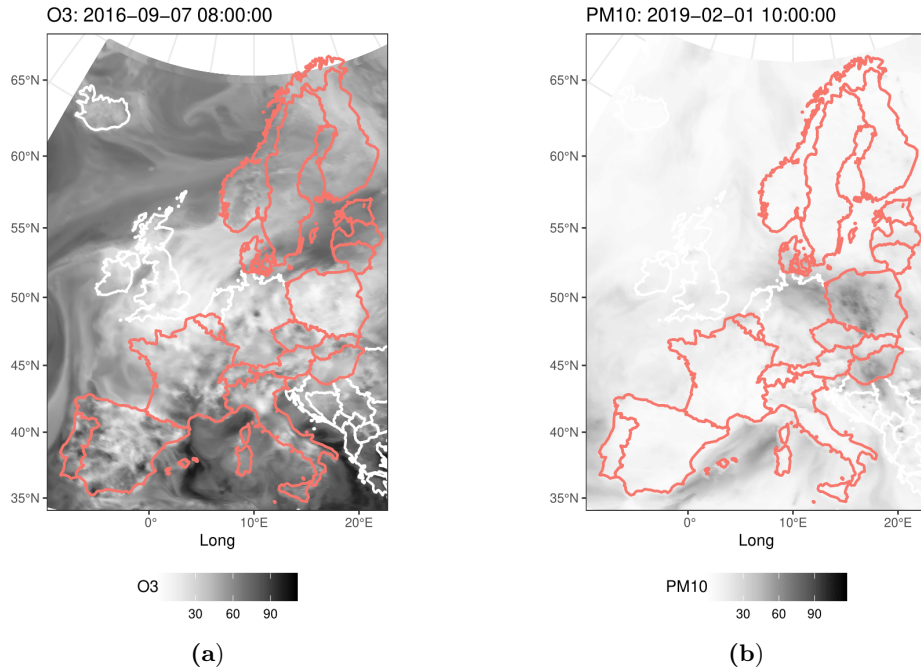


Figure 3: Panel (a) visualizes the ozone concentration on September 7, 2016 at 8:00 AM and panel (b) the PM10 concentration on February 1, 2019 at 10:00 AM. We highlight the boundaries of the 20 European countries under consideration.

3 Model specification

The proposed weekly mortality model aims to explain an excess or deficit of mortality, relative to a baseline mortality model, from environmental data. Hereto, the baseline mortality model estimates a weekly seasonal mortality pattern observed in the weekly mortality rates of each considered NUTS 3 region. As such, we obtain an estimate for the expected number of death counts in each week of the year and for each region, see Section 3.1. Mortality excess may arise from abnormal temperatures, elevated air pollution, or extreme humidity levels, among others. Therefore, we engineer features that quantify deviations from typical environmental conditions for each week of the year, referred to as anomalies. Furthermore, to allow for, e.g., heat waves or cold spells, we create extreme environmental indices that indicate how many days within a week a particular environmental feature exceeds a high quantile or is lower than a low quantile. We then use these environmental anomalies and extreme indices, along with lagged versions of them, to explain excess or deficit mortality relative to the mortality baseline, see Section 3.2.¹⁰ Section 5.1 provides a detailed discussion of the feature engineering step outlined above. To capture any complex interaction effects between the environmental features and their possibly non-linear impact on mortality, we employ a machine learning model. This offers the additional advantage of automating the feature selection process in a dataset with numerous features. Figure 4 illustrates the proposed methodology.

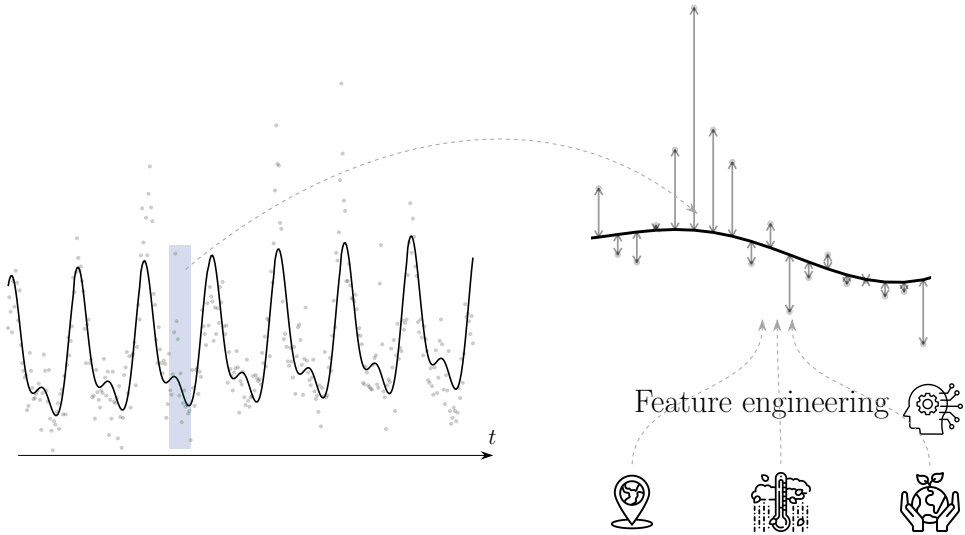


Figure 4: Visual representation of the proposed weekly mortality model, consisting of a baseline mortality model (left) and a machine learning model (right). The baseline model is region-specific and captures the overall seasonal pattern in the observed mortality rates. Next, we explain the mortality deviations from this region-specific baseline model with a machine learning algorithm using a set of engineered region-specific environmental features.

¹⁰Several feature engineering techniques exist in the literature. As an example, Nielsen et al. (2018) directly use the weekly average minimum and maximum temperatures to associate with excess mortality, and define weeks with extreme temperatures as those with mean temperatures above the expected maximum temperature. Gasparini and Armstrong (2011) construct a heat wave indicator by determining whether the average temperature exceeds a specified threshold value.

3.1 The baseline weekly mortality model

The weekly, region-specific baseline mortality model estimates the overall, seasonal trend observed in the region's weekly death counts, see Figure 1c for an example of this seasonality. We adhere to the framework proposed by Serfling (1963), incorporating seasonality through Fourier terms. We exclude the dependence on the age group x since our focus will be on the age group 65+, as motivated in Section 2.1. In this paper, we include population-exposures as an offset into a Poisson regression model. Hereto, we assume that the observed weekly death counts in region r are realizations from a Poisson distributed random variable $D_{t,w}^{(r)}$:

$$D_{t,w}^{(r)} \sim \text{Poisson} \left(E_{t,w}^{(r)} \mu_{t,w}^{(r)} \right), \quad (3.1)$$

and consider the following structure for $\mu_{t,w}^{(r)}$ for each region $r \in \mathcal{R}$ (Serfling, 1963):

$$\begin{aligned} \log \mu_{t,w}^{(r)} = & \beta_0^{(r)} + \beta_1^{(r)} t + \beta_2^{(r)} \sin \left(\frac{2\pi w}{52.18} \right) + \beta_3^{(r)} \cos \left(\frac{2\pi w}{52.18} \right) + \\ & \beta_4^{(r)} \sin \left(\frac{2\pi w}{26.09} \right) + \beta_5^{(r)} \cos \left(\frac{2\pi w}{26.09} \right), \end{aligned} \quad (3.2)$$

with 52.18 the average number of weeks per year.¹¹ Note that this baseline structure is region-, week-, and year-specific. Further, the region-specific parameters $\beta_p^{(r)}$, for $p = 0, 1, \dots, 5$, control for the level, trend, and seasonal variation. In Section 4.1, we show how to estimate this baseline model. We estimate the expected death counts from the baseline model in Equation (3.1) as:

$$\hat{b}_{t,w}^{(r)} := \hat{E} \left[D_{t,w}^{(r)} \right] = E_{t,w}^{(r)} \hat{\mu}_{t,w}^{(r)}, \quad (3.3)$$

for each region $r \in \mathcal{R}$, with $\hat{\mu}_{t,w}^{(r)}$ denoting the fitted baseline structure from Equation (3.2). The black solid line in the left panel of Figure 4 shows an example of this for one selected region.

3.2 Modeling mortality deviations from the baseline model

We aim to explain the deviations from the baseline expected death counts using short-term effects of a set of features engineered from the available region-specific environmental factors, as visualized in the right panel of Figure 4. Hereto, we treat the fitted baseline death counts, $\hat{b}_{t,w}^{(r)}$, obtained from Section 3.1, as fixed and use them as an offset in a predictive modeling technique. We impose the following distributional assumption:

$$\begin{aligned} D_{t,w}^{(r)} & \sim \text{Poisson} \left(\hat{b}_{t,w}^{(r)} \phi_{t,w}^{(r)} \right), \\ \phi_{t,w}^{(r)} & = f \left(\text{long}^{(r)}, \text{lat}^{(r)}, \text{season}_{t,w}, \mathbf{c}_{t,w}^{(r)}, \mathbf{e}_{t,w}^{(r)}, \right. \\ & \quad \left. l^1 \left(\mathbf{c}_{t,w}^{(r)} \right), l^1 \left(\mathbf{e}_{t,w}^{(r)} \right), \dots, l^s \left(\mathbf{c}_{t,w}^{(r)} \right), l^s \left(\mathbf{e}_{t,w}^{(r)} \right) \right). \end{aligned} \quad (3.4)$$

Here, $f(\cdot)$ denotes the outcome of a selected predictive model, such as a regression tree, random forest, gradient boosting, or neural network. Our preference for a machine learning model stems from its ability to highlight the important features from the high-dimensional set of environmental features, and to identify non-linear relationships of and potential interaction effects among the environmental features. $\mathbf{c}_{t,w}^{(r)}$ and $\mathbf{e}_{t,w}^{(r)}$ refer to the vectors of, respectively, the environmental

¹¹ Alternatively, the exact number of ISO weeks in the year of consideration can be used.

anomalies and extreme indices constructed for week $w \in \mathcal{W}_t$ of year $t \in \mathcal{T}$ in region $r \in \mathcal{R}$. These anomalies quantify deviations from region-specific baseline conditions, on which we further elaborate in Section 5.1. To enhance our analysis, we explicitly incorporate the longitude, i.e., $\text{long}^{(r)}$, and latitude coordinate, i.e., $\text{lat}^{(r)}$, of the centroid of each region r as well as the season, $\text{season}_{t,w} \in \{\text{Spring}, \text{Summer}, \text{Autumn}, \text{Winter}\}$, into the machine learning model.¹² This inclusion allows the learning method to take potential interaction effects into account between the region and the environmental features. For instance, the impact of temperature on mortality deviations from the baseline may differ between northern and southern regions. A similar rationale applies to seasonal effects. Lastly, we allow for lagged effects by including lagged values of the environmental features in the predictive model $f(\cdot)$. The functions $l^u(\cdot)$, for $u = 1, 2, \dots, s$, shift the features u weeks back in time. Lagged features play a crucial role in capturing various temporal phenomena and dependencies in data. For instance, they enable modeling the impacts on mortality of consecutive hot or cold weeks, consecutive elevated air pollution levels, and potential harvesting effects, among others (Schwartz, 2001). Harvesting effects occur when, for example, temperature related excess mortality in the previous week leads to a mortality deficit in the current week.

4 Calibration strategy and interpretation tools

4.1 Calibrating the baseline model

We calibrate the baseline weekly mortality model that captures the region-specific, seasonal pattern in the observed weekly death counts. Under the Poisson assumption from Equation (3.1) (Nelder & Wedderburn, 1972), we consider all regions and add a penalty term to obtain smooth variations in the estimated parameters $\hat{\beta}_p^{(r)}$ across neighbouring regions, for $p = 0, 1, \dots, 5$. Hereto, for notational convenience, we denote:

$$\begin{aligned} \boldsymbol{\beta}^{(r)} &:= (\beta_0^{(r)}, \beta_1^{(r)}, \beta_2^{(r)}, \beta_3^{(r)}, \beta_4^{(r)}, \beta_5^{(r)}) \in \mathbb{R}^{6 \times 1} \\ \mathbf{z}_{t,w} &:= \left(1, t, \sin\left(\frac{2\pi w}{52.18}\right), \cos\left(\frac{2\pi w}{52.18}\right), \sin\left(\frac{2\pi w}{26.09}\right), \cos\left(\frac{2\pi w}{26.09}\right)\right) \in \mathbb{R}^{6 \times 1}, \end{aligned}$$

where $\boldsymbol{\beta}^{(r)}$ represents the region-specific parameter vector, and $\mathbf{z}_{t,w}$ the covariate vector for week w in year t in the Poisson GLM, as detailed in Equations (3.1) and (3.2). Moreover, for $p = 0, 1, \dots, 5$, we write $\boldsymbol{\beta}_p$ to denote the parameter vector across the considered regions, i.e., $\boldsymbol{\beta}_p := (\beta_p^{(r)})_{r \in \mathcal{R}}$. We then calibrate the baseline weekly mortality model by minimizing the following objective function:

$$\hat{\boldsymbol{\beta}} = \underset{\boldsymbol{\beta}}{\operatorname{argmin}} -l_P(\boldsymbol{\beta}) + \sum_{p=0}^5 \lambda_p \boldsymbol{\beta}_p^T \mathbf{S} \boldsymbol{\beta}_p, \quad (4.1)$$

where $\boldsymbol{\beta} := (\boldsymbol{\beta}^{(r)})_{r \in \mathcal{R}}$ and $l_P(\boldsymbol{\beta})$ is the Poisson log-likelihood, defined, up to a constant, as:

$$l_P(\boldsymbol{\beta}) = \sum_{r \in \mathcal{R}} \sum_{t \in \mathcal{T}} \sum_{w \in \mathcal{W}_t} \left(d_{t,w}^{(r)} \cdot \left(\log E_{t,w}^{(r)} + (\boldsymbol{\beta}^{(r)})^T \mathbf{z}_{t,w} \right) - E_{t,w}^{(r)} \cdot \exp\left((\boldsymbol{\beta}^{(r)})^T \mathbf{z}_{t,w}\right) \right) \quad (4.2)$$

¹²We define the seasons as follows: spring covers March 15 to June 15; summer includes June 15 to September 15; autumn spans September 15 to December 15; and the winter encompasses December 15 to March 15. As our analysis focuses on weekly death counts, we define the season as the one in which the first day of the considered week falls.

with T the transpose operator, and where we assume that the $d_{t,w}^{(r)}$ are independent realizations from the Poisson distribution in Equation (3.1). Additionally, the objective function in Equation (4.1) contains penalty terms $\lambda_p \boldsymbol{\beta}_p^T \mathbf{S} \boldsymbol{\beta}_p$, for $p = 0, 1, \dots, 5$, to impose smooth variations in the parameter vector $\boldsymbol{\beta}_p$ across neighboring regions. Hereto, we use the following entries in the penalty matrix $S := (s_{ij})_{i,j}$, with $i, j \in \mathcal{R}$:

$$s_{ij} = \begin{cases} |\mathcal{N}_i| & \text{if } i = j \\ -1 & \text{if } i \neq j \text{ are neighboring regions} \\ 0 & \text{elsewhere,} \end{cases} \quad (4.3)$$

with \mathcal{N}_i the set of neighbors of region $i \in \mathcal{R}$. The smoothness penalty in Equation (4.3) leads to (see Appendix B):

$$\boldsymbol{\beta}_p^T \mathbf{S} \boldsymbol{\beta}_p = \sum_{i \in \mathcal{N}_1} (\beta_{p,1} - \beta_{p,i})^2 + \sum_{i \in \mathcal{N}_2 \setminus \{1\}} (\beta_{p,2} - \beta_{p,i})^2 + \dots + \sum_{i \in \mathcal{N}_{R-1} \setminus \{1, \dots, R-2\}} (\beta_{p,R-1} - \beta_{p,i})^2,$$

where, e.g., $\mathcal{N}_k \setminus \{1, \dots, k-1\}$ represents the set of neighbors of region k , excluding the first $k-1$ regions, for $k = 1, 2, \dots, R-1$. We hence observe that the imposed penalty matrix \mathbf{S} in Equation (4.3) penalizes the sum of the squared differences between the parameters of neighboring regions. Appendix B illustrates the construction of the smoothness matrix for a set of five Spanish NUTS 3 regions. The parameter λ_p in Equation (4.1) is a smoothing parameter controlling the degree of smoothness in the parameter $\boldsymbol{\beta}_p$ across neighboring regions. A very large λ_p results in the same $\beta_p^{(r)}$ across all regions, while a λ_p close to 0 results in no penalization on the parameter $\beta_p^{(r)}$, which corresponds to the parameters of a traditional, unregularized Poisson GLM. A similar smoothness technique has also been recently applied by [Li et al. \(2024\)](#) to shrink mortality forecasts in adjacent age groups and neighboring regions.

We estimate the parameters $\beta_p^{(r)}$ in Equation (4.1) using the penalized iteratively re-weighted least squares algorithm, where we select optimal smoothing parameters λ_p using Un-Biased Risk Estimation (UBRE) scores ([Wood, 2017](#)).¹³ We denote the optimal smoothing parameters as $\hat{\lambda}_p$, for $p = 0, 1, \dots, 5$, and the optimal parameter vector as $\hat{\boldsymbol{\beta}}$. We then estimate the expected baseline death counts for each region $r \in \mathcal{R}$, year $t \in \mathcal{T}$, and week $w \in \mathcal{W}_t$ as:

$$\hat{b}_{t,w}^{(r)} = E_{t,w}^{(r)} \cdot \exp \left(\left(\hat{\boldsymbol{\beta}}^{(r)} \right)^T \mathbf{z}_{t,w} \right). \quad (4.4)$$

4.2 Calibrating the mortality deviations model

Fixing the expected weekly baseline death counts, as obtained in Section 4.1, we now calibrate a predictive model to explain deviations from this baseline using environmental features. As discussed in Section 3.2, we employ a machine learning approach due to its capacity to handle high dimensional features, to capture non-linear relationships and to detect interactions among the environmental features. Machine learning algorithms typically rely on a set of parameters of which some are carefully selected through a tuning process (tuning parameters), while others are set to predetermined values (hyper-parameters). In this paper, we opt for an extensive grid search that involves exploring a predefined grid of parameter values to identify optimal tuning parameter configurations.

¹³We use the argument `paraPen` from the `gam` function in the R-package `mgcv` to implement the proposed spatially smoothed Poisson GLM, see [Wood \(2015\)](#).

XGBoost algorithm. While any predictive modeling technique can be deployed in our framework, we will specifically focus on the extreme gradient boosting machine (Chen & Guestrin, 2016) in the case study outlined in Section 5. Appendix D.1 explains the XGBoost algorithm in case of a Poisson distributed outcome, see Equation (3.4), and details the considered tuning parameters. We hereby choose the negative Poisson log-likelihood as the loss function:

$$\mathcal{L} \left(d_{t,w}^{(r)}, \hat{d}_{t,w}^{(r)} \right) = \hat{b}_{t,w}^{(r)} \cdot f \left(\mathbf{x}_{t,w}^{(r)} \right) - d_{t,w}^{(r)} \cdot \left(\log f \left(\mathbf{x}_{t,w}^{(r)} \right) + \log \hat{b}_{t,w}^{(r)} \right) + \log d_{t,w}^{(r)}!, \quad (4.5)$$

for $r \in \mathcal{R}$, $t \in \mathcal{T}$ and $w \in \mathcal{W}_t$. Here, $\hat{d}_{t,w}^{(r)} = \hat{b}_{t,w}^{(r)} \cdot f(\mathbf{x}_{t,w}^{(r)})$ is the estimated death count in week w of year t for region r , and $\mathbf{x}_{t,w}^{(r)}$ is the input vector of the XGBoost model consisting of the (lagged) weather anomalies and extreme weather indices $\mathbf{c}_{t,w}^{(r)}$, the (lagged) air pollution anomalies and extreme air pollution indices $\mathbf{e}_{t,w}^{(r)}$, the season $\text{season}_{t,w}$ and the longitude $\text{long}^{(r)}$ and latitude $\text{lat}^{(r)}$ coordinates, see Equation (3.4) in Section 3.2.

Parameter tuning with cross-validation. We use K -fold cross-validation to select optimal values for the six tuning parameters listed in Table D.1, inspired by Hastie et al. (2001).¹⁴ For simplicity, let $\mathcal{T} = \{0, 1, 2, \dots, T-1\}$ represent the considered time range consisting of T years. We choose the number of folds (K) to be equal to the number of years in our training data, i.e., $K = T$. Each fold uses a specific year $t \in \mathcal{T}$ as validation data and the remaining years as training data. Consequently, for each fold, the validation data consists of either $53 \cdot |\mathcal{R}|$ observations for a leap year or $52 \cdot |\mathcal{R}|$ observations otherwise. Appendix D.2 describes the tuning strategy in further detail, with a visualisation in Figure D.1. The optimal tuning parameters correspond to the parameter combination that yields the smallest average Poisson negative log-likelihood on the hold-out folds.

Training Using the optimally chosen values for the tuning parameters, we calibrate the XGBoost model on the available historical data covering the entire duration of T years. We denote the outcomes estimated from the XGBoost model as $\hat{f}_{\text{XGBoost}} \left(\mathbf{x}_{t,w}^{(r)} \right)$ for $r \in \mathcal{R}$, $t \in \mathcal{T}$ and $w \in \mathcal{W}_t$. Consequently, the estimated death counts equal:

$$\hat{d}_{t,w}^{(r)} = \hat{b}_{t,w}^{(r)} \cdot \hat{f}_{\text{XGBoost}} \left(\mathbf{x}_{t,w}^{(r)} \right), \quad r \in \mathcal{R}, t \in \mathcal{T}, w \in \mathcal{W}_t.$$

As such, we can interpret the outcomes from the XGBoost model as a multiplier that can either augment or diminish the baseline number of death counts.

4.3 Interpretation tools

Machine learning algorithms, like the XGBoost model, are often seen as black boxes. Therefore, the use of interpretation tools becomes crucial to unravel insights from these black box algorithms (Molnar, 2019). We assume that the training data, i.e.,

$$\left\{ \left(\mathbf{x}_{t,w}^{(r)}, \hat{b}_{t,w}^{(r)}, d_{t,w}^{(r)} \right) \right\}_{r \in \mathcal{R}, t \in \mathcal{T}, w \in \mathcal{W}_t}, \quad (4.6)$$

¹⁴See Bergmeir et al. (2018) for a discussion on why traditional K-fold cross-validation can be used in a time series setting, conditionally on the lag structure in the model being adequately specified. Moreover, by incorporating the baseline number of deaths as an offset in our machine learning model, we effectively eliminate the trend and seasonal components from the time series of death counts, and, as such, enhance the applicability of traditional cross-validation techniques.

consists of feature vectors with q variables:

$$\mathbf{x}_{t,w}^{(r)} = \left(x_{1,t,w}^{(r)}, x_{2,t,w}^{(r)}, \dots, x_{q,t,w}^{(r)} \right) \in \mathbb{R}^q.$$

For simplicity, we refer in the below explanation to X_l as the l -th feature, for $l = 1, \dots, q$, as random variable and to $f(\cdot)$ as the fitted XGBoost model $\hat{f}_{\text{XGBoost}}(\cdot)$.

Feature importance In this interpretation tool, our objective is to unveil the features that significantly contribute to the predictions. We follow the approach proposed by [Breiman and Ihaka \(1984\)](#) and measure the importance of a particular feature X_l within a regression tree by aggregating the reductions in the considered loss function across all splits associated to this feature. Given that the XGBoost model consists of multiple regression trees, see Appendix D.1, we extend this analysis to measure the reduction in loss caused by feature X_l across all trees in the ensemble. Appendix D.3 outlines the mathematical formulation of the feature importance. The higher the feature importance, the more important the feature is to the prediction process.

Accumulated Local Effects [Apley and Zhu \(2020\)](#) propose Accumulated Local Effects (ALE) plots to visualize the impact of a particular feature on the predictions generated by a machine learning model. In contrast to the partial dependence plots introduced by [Friedman \(2001\)](#), ALE plots prove to be more effective in illustrating feature effects when dealing with correlated features ([Molnar, 2019](#)). Given the strong correlation present in the environmental features, this paper places specific emphasis on the relevance of ALE plots for visualizing and interpreting the impact of a feature on the predictions. Appendix D.3 outlines the mathematical formulation and technical details of ALE effects.

5 Case study on the NUTS 3 regions in 20 European countries

5.1 Feature engineering

To examine the short-term association between environmental factors and weekly mortality rates, we use data on weekly death counts for the age group 65+ within the NUTS 3 geographical regions for the years 2013-2019, as detailed in Section 2.2. Hereto, we first aggregate the temporal and spatial dimensions of the gridded, environmental data into daily features, registered at NUTS 3 level, see Sections 5.1.1 and 5.1.2 respectively. To capture the effects of extreme environmental conditions, such as heat waves and cold spells, we engineer extreme environmental indices that indicate how many days within a week the environmental factors exceed a certain high quantile or are lower than a certain low quantile (see Section 5.1.3). Furthermore, since the focus in this paper is on explaining short-term deviations from a baseline model for weekly death counts, we also engineer environmental anomalies that quantify deviations from normal, baseline conditions for each week in the year (see Section 5.1.4). Lastly, we aggregate the environmental features on a weekly basis and create lagged versions of it in Section 5.1.5. Figure 5 illustrates the feature engineering process for the weather related factors listed in Table 1 and the air pollution factors in Table 2. The flow chart refers to the section that further details each step at the upper right corner of the corresponding box.

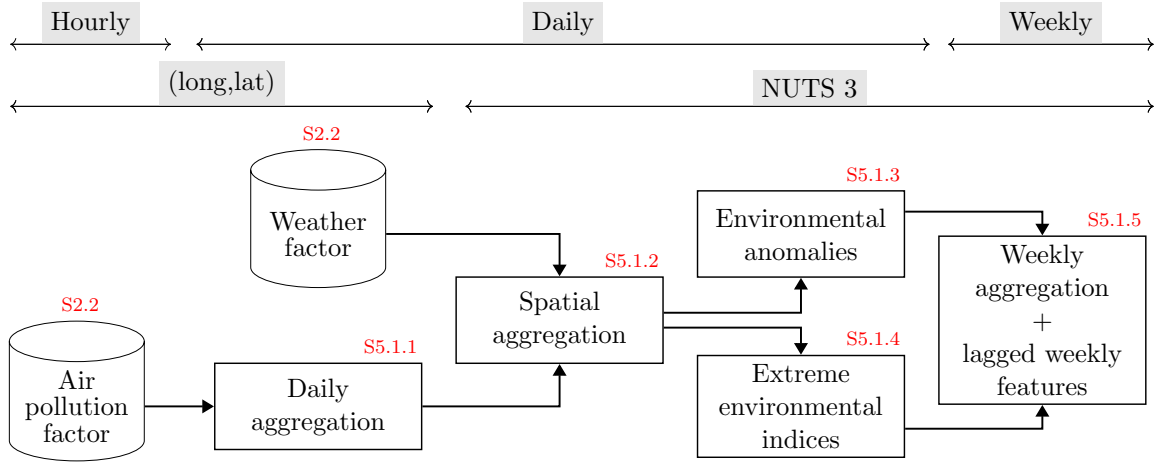


Figure 5: Flow chart explaining the feature engineering process for the weather-related factors and the air pollution factors, with the relevant section that details each step at the upper right corner of the box.

5.1.1 Daily aggregation of hourly air pollutant levels

We consider an air pollution factor from Table 2 and denote it as $x_{t,w,d,h}^{(\text{long},\text{lat})}$. This feature represents the concentration of a specific air pollutant in year t , week w , day d , and hour h , located at longitude-latitude coordinates (long,lat) . We then compute the daily minimum, average, and maximum concentrations of the air pollutant, measured at the coordinates (long,lat) as follows:

$$\begin{aligned}\hat{x}_{t,w,d}^{(\text{long},\text{lat})} &= \min \left\{ x_{t,w,d,h}^{(\text{long},\text{lat})} \mid h = 0, 1, \dots, 23 \right\} \\ \bar{x}_{t,w,d}^{(\text{long},\text{lat})} &= \text{avg} \left\{ x_{t,w,d,h}^{(\text{long},\text{lat})} \mid h = 0, 1, \dots, 23 \right\} \\ \vee_{t,w,d}^{(\text{long},\text{lat})} &= \max \left\{ x_{t,w,d,h}^{(\text{long},\text{lat})} \mid h = 0, 1, \dots, 23 \right\}.\end{aligned}$$

For the weather factors listed in Table 1, we do not need to make the conversion from an hourly to a daily time scale, since these factors are already defined on a daily time scale at specific longitude-latitude coordinates.

5.1.2 Population-weighted spatial aggregation to NUTS 3 level

Let $\tilde{x}_{t,w,d}^{(\text{long},\text{lat})}$ denote the measurement of a particular environmental factor at coordinates (long,lat) , year t , week w , and day d . This feature can encompass minimum, maximum, or average air pollution measurements, as defined in Section 5.1.1, or any weather-related factor from Table 1.

We consider the grid \mathcal{G} of longitude-latitude coordinates (long,lat) on which the feature $\tilde{x}_{t,w,d}^{(\text{long},\text{lat})}$ is registered. We then introduce the function:

$$m_{\mathcal{G}} : \mathcal{G} \rightarrow \mathcal{R} : (\text{long},\text{lat}) \mapsto r,$$

which maps longitude-latitude coordinates from the grid \mathcal{G} to the NUTS 3 region r it belongs. Now, define the set $\mathcal{I}(r)$ that consists of all (long,lat) coordinates of the grid \mathcal{G} contained in the NUTS 3 region r :

$$\mathcal{I}(r) = \{(\text{long},\text{lat}) \in \mathcal{G} \mid m_{\mathcal{G}}(\text{long},\text{lat}) = r\}. \quad (5.1)$$

We create a weighted aggregated feature at the NUTS 3 geographical level as follows:

$$\tilde{x}_{t,w,d}^{(r)} = \sum_{(\text{long,lat}) \in \mathcal{I}(r)} \omega_{(\text{long,lat})} \cdot \tilde{x}_{t,w,d}^{(\text{long,lat})}, \quad (5.2)$$

where $\omega_{(\text{long,lat})}$ are weights that sum up to one within each grid $\mathcal{I}(r)$. These weights aim to compute a population-weighted version of the daily environmental factors, a method that has also been explored in the existing literature (Balakrishnan et al., 2019; de Schrijver et al., 2021). This weighting strategy is necessary due to the uneven distribution of a population within a NUTS 3 region, which tends to concentrate around specific locations. Therefore, we put more weight on the daily measurements of the environmental factors at longitude-latitude coordinates where more people are located, relative to the population in that NUTS 3 region. We assume these weights $\omega_{(\text{long,lat})}$ to remain constant over time. This assumption is consistent with the idea that the proportion of the population within region r associated with grid point $(\text{long,lat}) \in \mathcal{I}(r)$ remains relatively stable throughout the time span under consideration.¹⁵

We compute the weights using the Socioeconomic Data and Applications Center (SEDAC) in NASA's Earth Observing System Data and Information System (EOSDIS).¹⁶ Particularly, we use the high-dimensional population count dataset, defined on a grid with a spatial resolution of 2.5 arc-minutes (≈ 5 km) and a temporal dimension of five years (CIESIN et. al, 2018). We extract the population gridded dataset at the year 2015 to construct the population weights in Equation (5.2).¹⁷ Appendix C.1 details the strategy on how to compute the population weights, with a visualisation in Figure C.1.¹⁸

5.1.3 Daily extreme environmental indices

To capture the effects of extreme environmental conditions on mortality, we construct daily, region-specific features that indicate whether the daily, environmental measurement in that region exceeds a certain high quantile or falls below a certain low quantile. This quantile-based approach has been previously used in the literature to analyze the effects of heat waves (Anderson & Bell, 2009; Gasparrini & Armstrong, 2011; Hajat et al., 2006). Hereto, we propose to calculate the region-specific 5% and 95% quantile of the entire set of historical observations on the daily minimum temperature T_{\min} , the average temperature T_{avg} , and the maximum temperature T_{\max} throughout the considered time period 2013-2019. We define the extreme high temperature index for region r on day d in week w of year t as:

$$T.\text{ind}_{t,w,d}^{(r,95\%)} = \mathbb{1} \left\{ T_{\max}^{(r)}_{t,w,d} \geq q_{T_{\max}}^{(r,95\%)} \right\} + \mathbb{1} \left\{ T_{\text{avg}}^{(r)}_{t,w,d} \geq q_{T_{\text{avg}}}^{(r,95\%)} \right\} + \mathbb{1} \left\{ T_{\min}^{(r)}_{t,w,d} \geq q_{T_{\min}}^{(r,95\%)} \right\}, \quad (5.3)$$

with, e.g., $\mathbb{1}\{T_{\max}^{(r)}_{t,w,d} \geq q_{T_{\max}}^{(r,95\%)}\}$ an indicator function which equals one when the maximum temperature in region r on day d in week w of year t exceeds its historical 95% quantile, and zero otherwise. We refer to this feature as the hot-day index. The index can take values 0, 1, 2, or 3, where a value of three corresponds to a very hot day. We define a similar cold-day index using the 5% quantile, where a value of three corresponds to a very cold day. Similarly, we create daily indices for surpassing high thresholds of the other environmental factors and refer to them as extreme environmental indices.

¹⁵Our current method assigns each grid point $(\text{long,lat}) \in \mathcal{G}$ exclusively to one NUTS 3 region r . Alternatively, an interpolation method could be explored, enabling grid points near the borders of NUTS 3 regions to also contribute to the calculation of the feature at NUTS 3 level in Equation (5.2).

¹⁶This data center is available on <https://sedac.ciesin.columbia.edu/>.

¹⁷We select the year 2015 since it falls within our considered time range.

¹⁸In Appendix C.1, we denote the feature grid as $\mathcal{G}^{(1)}$ and the population grid as $\mathcal{G}^{(2)}$. Additionally, we represent the feature grid and the population grid restricted to a NUTS 3 region r by $\mathcal{I}_1(r)$ and $\mathcal{I}_2(r)$, respectively.

5.1.4 Daily environmental anomalies

Alongside the extreme environmental indices, constructed in Section 5.1.3, we engineer environmental anomalies that measure deviations from daily baseline conditions, see, e.g., (Ballester et al., 2023) for an application of temperature anomalies to estimate the heat-related mortality during the summer of 2022 in European regions. Some of the daily environmental features exhibit a clear seasonal pattern. For these features, we first fit a region-specific baseline model using robust linear regression with a single set of sine and cosine Fourier terms as covariates (Gervini & Yohai, 2002).¹⁹ In this way, we capture the region-specific baseline environmental conditions on each day within a year. We have:

$$\tilde{x}_{t,w,d}^{(r)} = \alpha_0^{(r)} + \alpha_1^{(r)} \sin\left(\frac{2\pi \text{day}_{t,w,d}}{365.25}\right) + \alpha_2^{(r)} \cos\left(\frac{2\pi \text{day}_{t,w,d}}{365.25}\right) + \epsilon_{t,w,d}^{(r)}, \quad (5.4)$$

where $\epsilon_{t,w,d}^{(r)}$ is a normally distributed error term, $\text{day}_{t,w,d}$ denotes the number of the day in year t for ISO-date (t, w, d) , and 365.25 represents the average number of days per year.²⁰ In case a feature does not exhibit a clear annual, seasonal pattern, we do not consider a baseline model for that feature.

Figure 6 shows an example of the daily baseline trend for three weather factors as registered in three different NUTS 3 regions. Figure 6a visualizes the seasonal baseline trend for the daily maximum temperature levels in Barcelona (ES511), showing higher maximum temperatures during summer days compared to winter days. Figure 6b shows the seasonal baseline trend for the daily wind speed levels. Furthermore, we assume a zero baseline trend for the variable Rain, visualized by the blue line in Figure 6c. In the remainder of this section, we will work with the excesses or deviations from the baseline levels, also referred to as anomalies. These anomalies are the residuals from the region-specific baseline in Equation (5.4) for the different environmental features. The anomalies of an environmental feature $\tilde{x}_{t,w,d}^{(r)}$ with a non-zero baseline equal:

$$\Delta \tilde{x}_{t,w,d}^{(r)} = \tilde{x}_{t,w,d}^{(r)} - \hat{\tilde{x}}_{t,w,d}^{(r)},$$

where $\hat{\tilde{x}}_{t,w,d}^{(r)}$ represents the estimated daily baseline environmental condition in region r at day d of week w in year t . In case of a zero baseline trend, i.e., for wind speed, we take $\Delta \tilde{x}_{t,w,d}^{(r)} = \tilde{x}_{t,w,d}^{(r)}$.

5.1.5 Weekly averages of daily environmental anomalies and extreme indices

We align the daily time scale of the environmental anomalies (see Section 5.1.4) and the extreme environmental indices (see Section 5.1.3), with the weekly time scale of the death counts. Hereto, let $\tilde{a}_{t,w,d}^{(r)}$ be any environmental anomaly or extreme environmental index, registered in region r at day d of week w in year t . We then compute the weekly averages of this environmental feature as:

$$\bar{a}_{t,w}^{(r)} = \text{avg} \left\{ \tilde{a}_{t,w,d}^{(r)} \mid d = 1, 2, \dots, 7 \right\},$$

for all $t \in \mathcal{T}$, $w \in \mathcal{W}_t$, and $r \in \mathcal{R}$. This weekly averaging process captures effects such as the heightened impact of prolonged periods of environmental stress on mortality rates, e.g., multiple hot days within a week. Table 3 lists the final features which we use as inputs in the machine learning model. Alongside these features, we also introduce the lagged feature values, using the suffix `_11`, e.g., `w_avg_Tmax_anom_11`.

¹⁹By adopting robust linear regression, the fitted baseline model becomes less susceptible to the impact of extreme levels within the observed environmental features. We use the `lmRob` function in the R-package `robust`.

²⁰Alternatively, the exact number of days in a year can be used, with 366 days in a leap year and 365 days otherwise.

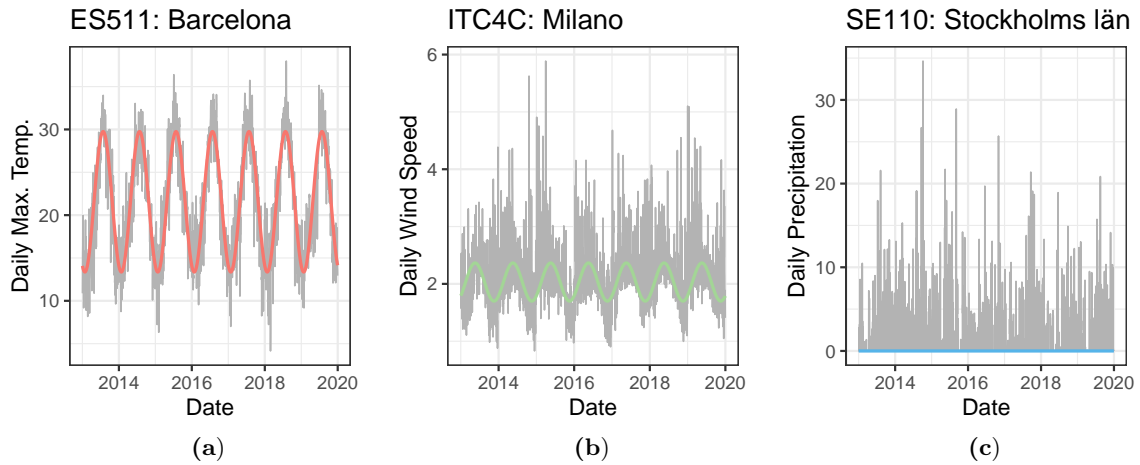


Figure 6: We visualize the baseline model across the years 2013-2019, fitted by means of robust linear regression with one sine-cosine Fourier pair for the daily maximum temperatures observed in Barcelona (a) and for the daily wind speed levels in Milano (b). In panel (c), we show the daily precipitation amounts in Stockholm with a zero baseline trend.

Feature	Weekly average of the daily	Feature	Weekly average of the daily
w_avg_Tmax_anom	maximum temperature anomalies	w_avg_O3_anom	average ozone anomalies
w_avg_Tmin_anom	minimum temperature anomalies	w_avg_O3.ind95	high ozone index
w_avg_T.ind95	hot-day index, see Equation (5.3)	w_avg_O3.ind5	low ozone index
w_avg_T.ind5	cold-day index	w_avg_N02_anom	average nitrogen dioxide anomalies
w_avg_Hum_anom	average relative humidity anomalies	w_avg_N02.ind95	high nitrogen dioxide index
w_avg_Hum.ind95	high humidity index	w_avg_N02.ind5	low nitrogen dioxide index
w_avg_Hum.ind5	low humidity index	w_avg_PM10_anom	average PM10 anomalies
w_avg_Rain	total precipitation levels	w_avg_PM10.ind95	high PM10 index
w_avg_Rain.ind95	high precipitation index	w_avg_PM10.ind5	low PM10 index
w_avg_Rain.ind5	low precipitation index	w_avg_PM2.5_anom	average PM2.5 anomalies
w_avg_Wind_anom	average wind speed anomalies	w_avg_PM2.5.ind95	high PM2.5 index
w_avg_Wind.ind95	high wind speed index	w_avg_PM2.5.ind5	low PM2.5 index
w_avg_Wind.ind5	low wind speed index		

Table 3: Weekly region-specific, environmental features at a NUTS 3 geographical level. The notation is as follows: `w_avg` refers to ‘weekly average’, `anom` denotes ‘daily anomalies’, `ind95` and `ind5` indicate, respectively, the extreme indicator at the 95% and 5% quantile. For example, `w_avg_Tmax_anom` represents the weekly average of the daily maximum temperature anomalies. `w_avg_Rain` represents the weekly average of daily precipitation levels, considering a zero baseline trend, as detailed in Section 5.1.4.

Figure 7 illustrates the correlations among the weekly environmental features, as detailed in Table 3. The most notable positive correlations appear between the weekly averages of daily PM2.5 and PM10 anomalies (0.95), and between the weekly averages of daily maximum and minimum temperature anomalies (0.73). Additionally, unsurprisingly, strong positive correlations are observed between the weekly averages of various environmental anomalies and their respective high quantile indices. Conversely, notable negative correlations emerge between the weekly averages of daily environmental anomalies and their corresponding low quantile indices.

Figure 8 presents the weekly aggregated features at the NUTS 3 level during the 30th ISO week of 2018. Figure 8a illustrates the weekly average of the daily maximum temperature anomalies (`w_avg_Tmax_anom`), while Figure 8b depicts the weekly average of the daily hot day index (`w_avg_T.ind95`). In Figure 8c, we show the weekly average of the daily average relative humidity anomalies (`w_avg_Hum.anom`), and Figure 8d displays the weekly average of the daily

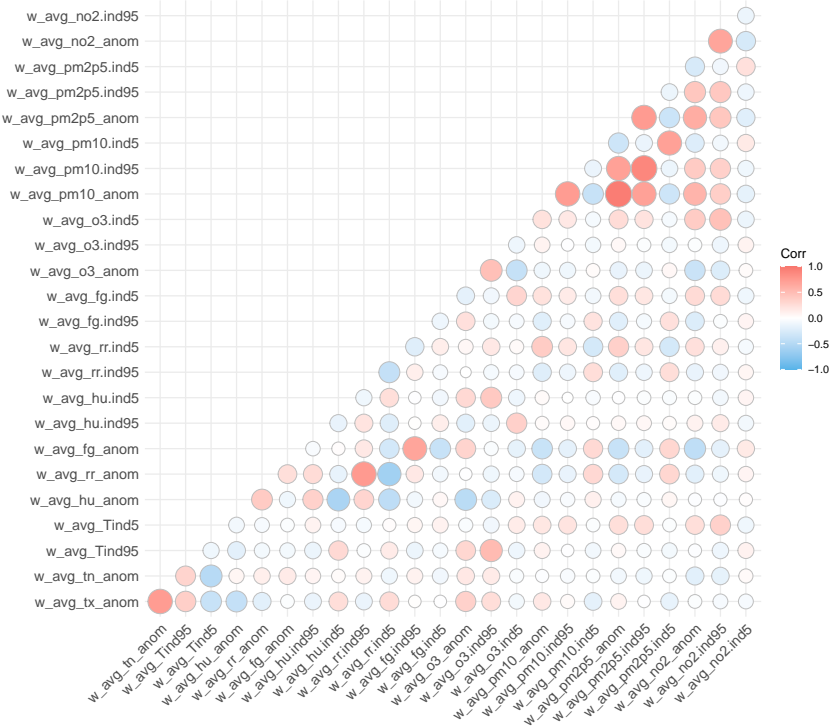


Figure 7: Correlations between the weekly environmental features, constructed through the feature engineering process in Figure 5, and presented in Table 3.

average ozone anomalies (`w_avg_o3.anom`). We conclude from Figure 8a that the 30th ISO week of 2018 exhibited significantly elevated temperatures in the Nordic countries and the northern regions of France, surpassing region-specific baseline maximum temperature levels by more than six degrees. A similar analysis for the weekly hot-day index reveals heightened values in the northern regions, indicating not only high daytime temperatures but also warmer-than-normal nights (see Figure 8b). In terms of humidity, Figure 8c shows lower-than-baseline levels in Central European regions, while southern regions exhibited higher humidity levels. This is consistent with the typical negative correlation between temperature and humidity (Fischer & Knutti, 2013). Furthermore, the northern French and Belgian regions exhibited higher ozone levels compared to baseline concentrations, as Figure 8d suggest.

5.2 Calibration

5.2.1 Calibrating the baseline model for weekly death counts

We calibrate the baseline model for weekly death counts, as outlined in Equations (3.1) and (3.2), by minimizing the penalized Poisson negative log-likelihood, as discussed in Section 4.1. This penalization ensures a smooth variation of the fitted parameters $\beta_p^{(r)}$ in the baseline model across neighboring regions, which is particularly useful for regions with a low number of weekly death counts. We consider the calibration period $\mathcal{T} = \{2013, 2014, \dots, 2019\}$.

Figure 9 illustrates the fitted parameters in the spatially smoothed baseline model, showing smooth variations in the parameters between adjacent regions. The estimated parameter $\hat{\beta}_1^{(r)}$ for the ISO year effect exhibits a negative sign in northern European regions and a slightly positive sign in southern regions. This suggests that, from 2013 to 2019, mortality rates slightly

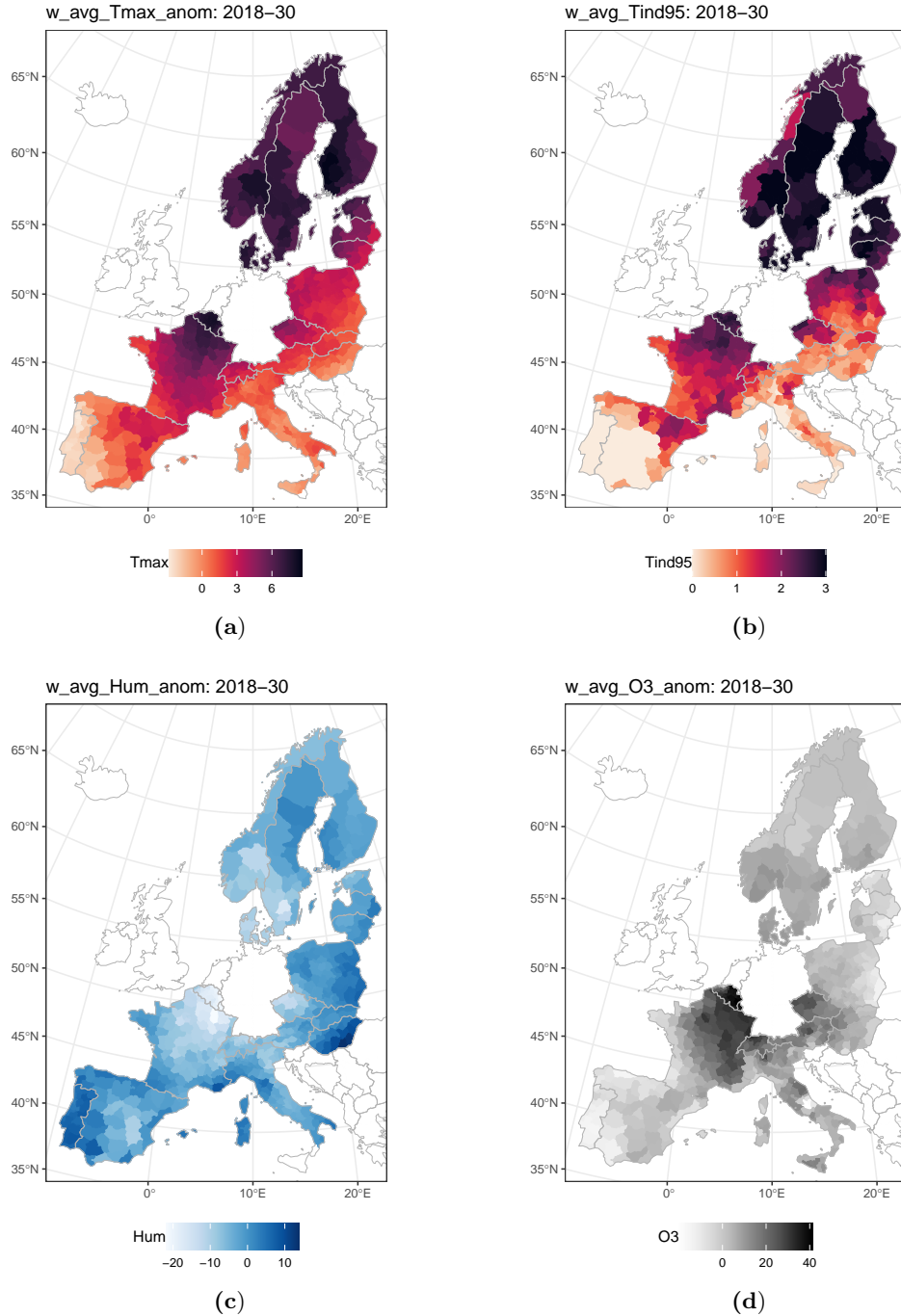


Figure 8: Weekly average of the daily maximum temperature anomalies (a), daily hot day index (b), daily average relative humidity anomalies (c), and daily average ozone anomalies (d) in the 30th ISO week of the year 2018 in the NUTS 3 European regions.

increased in the south while declining in the north. Moreover, the larger magnitude of the estimated parameters related to the sine and cosine Fourier terms in southern regions suggests that the associated seasonal patterns (with 52-week or 26-week periods) have a more pronounced effect on weekly death counts in southern regions compared to northern regions.

Figure 10a illustrates the estimated baseline mortality rates $\hat{q}_{t,w}^{(r)}$ in red, as obtained from Equation (2.1) when using the estimated force of mortality specified in Equation (3.2). In line with

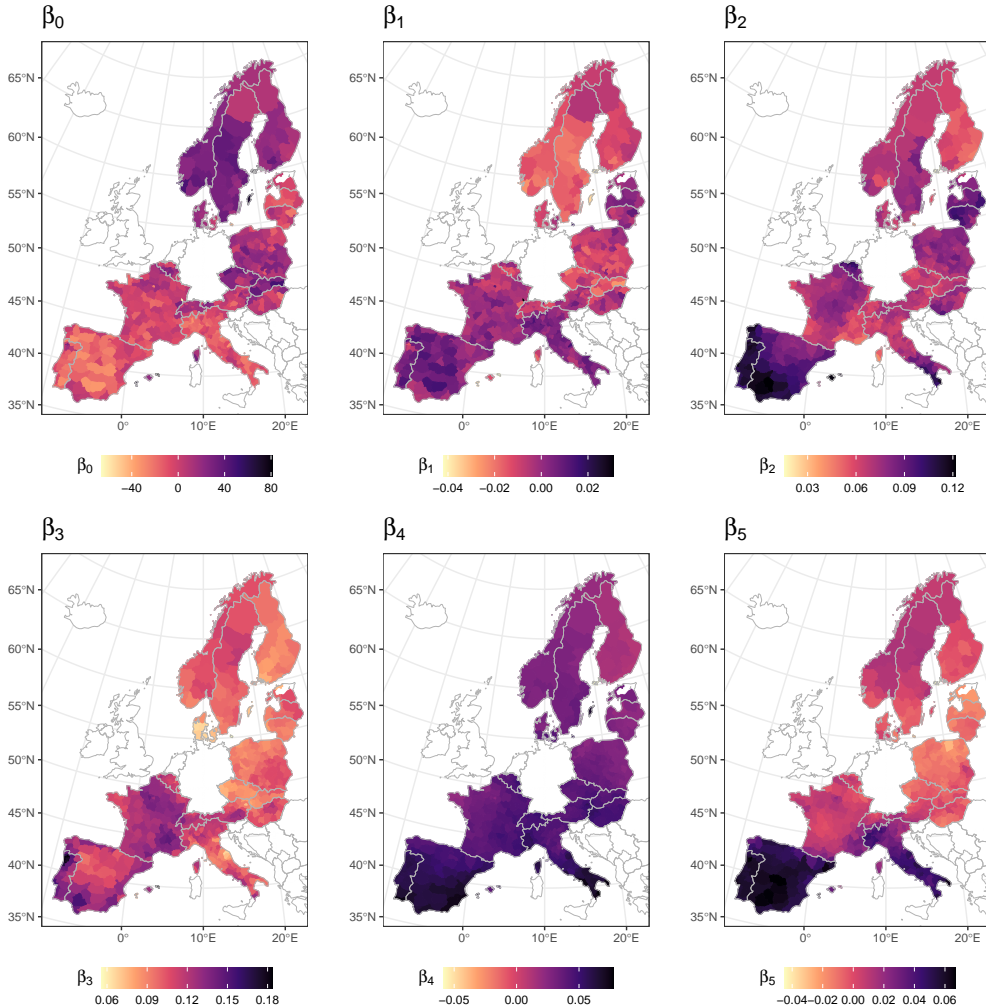


Figure 9: The fitted parameters $\hat{\beta}_0^{(r)}$, $\hat{\beta}_1^{(r)}$, and $\hat{\beta}_2^{(r)}$ (top panels) and $\hat{\beta}_3^{(r)}$, $\hat{\beta}_4^{(r)}$, and $\hat{\beta}_5^{(r)}$ (bottom panels) in the spatially smoothed Poisson GLM belonging to the intercept, ISO year t and the sine and cosine Fourier terms with a period of 52 or 26 weeks, see Equation (3.2).

the findings from Figure 9, we observe, for example, that the seasonal variation in Barcelona is more pronounced than in Milano and Stockholm. Furthermore, the mortality rates in the southern regions show a relatively stable (Barcelona) or slightly increasing (Milano) trend, whereas the mortality rates in the region of Stockholm clearly exhibit a decreasing trend.

5.2.2 Tuning and calibrating the machine learning model

After the calibration of the baseline model for the weekly death counts in Section 5.2.1, we now focus on calibrating the XGBoost model as explained in Section 4.2. This machine learning model incorporates the environmental features engineered in Section 5.1 and listed in Table 3. Additionally, we incorporate the one-week lagged values of the features in Table 3 and the `season`. We furthermore allow for spatial variations in the impact of specific features on the weekly deviations from the baseline death counts by incorporating the longitude (`long`) and latitude (`lat`) coordinates of the centre of each NUTS 3 region. This leads to a total of 56 features used as inputs in the machine learning model.

We consider the following tuning grid for the six XGBoost parameters of interest:

$$\begin{aligned} \text{nrounds} &\in \{10, 20, \dots, 5000\}, \quad \text{eta} \in \{0.01, 0.05, 0.1\}, \quad \text{min_child_weight} \in \{10, 100, 1000\} \\ \text{subsample} &\in \{0.50, 0.75\}, \quad \text{colsample_bytree} \in \{0.50, 0.75\}, \quad \text{max.depth} \in \{1, 3, 5, 7, 9\}. \end{aligned}$$

We tune these six parameters by means of 7-fold cross-validation, following the approach outlined in Section 4.2.²¹ Throughout this cross-validation process, the offset, representing the estimated baseline deaths, is considered to be known. While, in principle, we should recalibrate this offset for each set of training fold combinations, we refrain from doing so due to computational constraints. Moreover, the robust construction of the baseline model ensures that excluding one year from the training set will only have a negligible impact on the baseline fit and consequently on the offset.

The optimal set of tuning parameters, see Table D.1, consists of 490 boosting iterations (`nrounds`), a learning rate of 0.01 (`eta`), a minimum child weight of 1 000 (`min_child_weight`), a maximum depth of 7 for each tree (`max.depth`), and a subsample ratio of 75% and 50% for the training data (`subsample`) and the columns (`colsample_bytree`), respectively. Subsequently, we retrain the machine learning model using this optimal parameter set over the entire calibration period spanning the years 2013-2019.

5.3 Model fits, findings and discussion

5.3.1 In-sample fit and model performance

Figure 10a displays the observed mortality rates in grey, alongside the estimated mortality rates from both the baseline model (red) and the machine learning model integrating environmental features (blue). The comparison reveals that the machine learning model performs better in terms of an in-sample fit compared to the baseline model. In Barcelona and Milano, the proposed model effectively captures the excess mortality during the winters of 2015/2016 and 2017/2018, and the excess mortality observed during the summer of 2015. In Stockholm, the model identifies the excess mortality observed during the summer of 2014 and 2018. These findings are confirmed by Figure 10b, which visualizes the residuals corresponding to the estimated mortality rates, calculated as:

$$\text{resid}_{t,w}^{(r)} = \hat{q}_{t,w}^{(r)} - q_{t,w}^{(r)},$$

where $\hat{q}_{t,w}^{(r)}$ and $q_{t,w}^{(r)}$ represent the estimated and observed mortality rate in week w of year t in region r , respectively. The estimated mortality rate is derived from either the baseline or the machine learning model (XGBoost). We observe less peaks in the residuals of the machine learning model compared to the residuals of the baseline model, particularly during the summer and winter weeks.

5.3.2 Interpretation tools

Feature importance. We analyze which features contribute most to the machine learning model that captures deviations in mortality from the baseline model. Hereto, we use the feature importance measure outlined in Section 4.3. Figure 11 presents the features with a feature importance exceeding 1%. To illustrate the variability in these feature importance measures, we

²¹We consider a 7-fold cross-validation as the calibration period \mathcal{T} consists of seven years, i.e., the years 2013-2019.

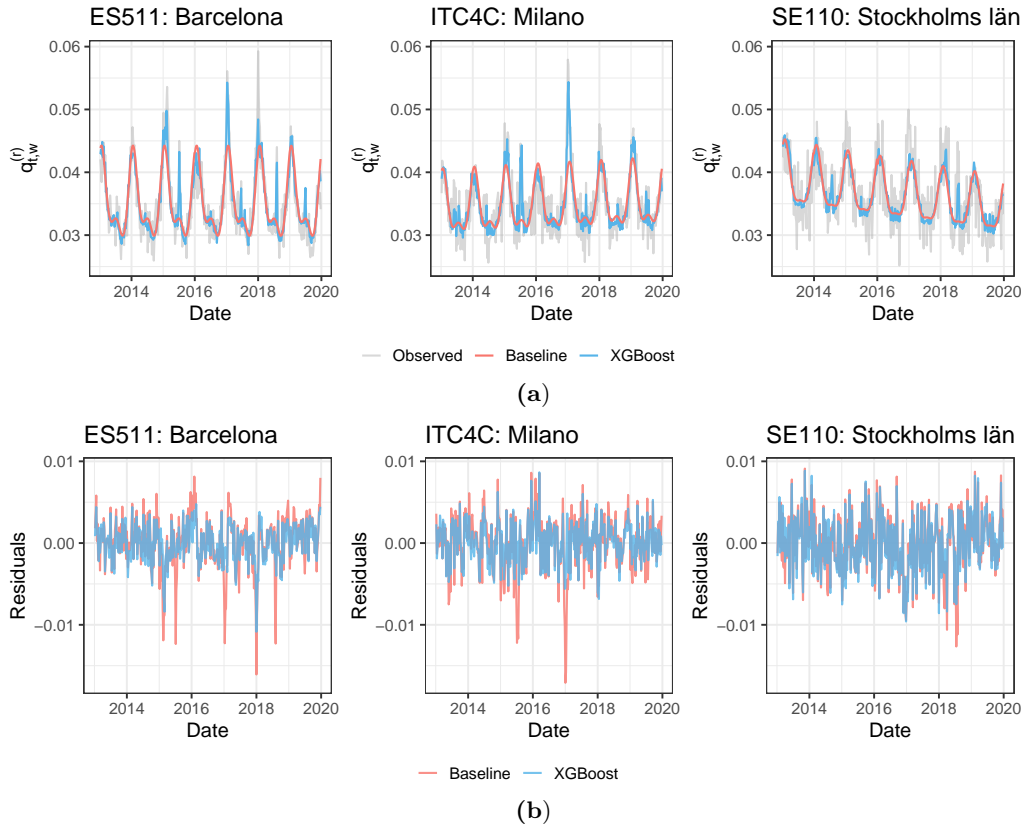


Figure 10: Panel (a): the observed and estimated weekly mortality rates during the period 2013-2019 in the NUTS 3 regions of Barcelona (left), Milano (middle), and Stockholm (right). The observed weekly mortality rates are shown in grey and the mortality rates as obtained from the baseline model and the XGBoost model in red and blue, respectively. Panel (b): residuals of the estimated weekly mortality rates derived from the baseline model (red) and the XGBoost model (blue) in Barcelona (left), Milano (middle), and Stockholm (right).

create 1 000 bootstrap copies of the same size as the training data.²² We then recalibrate the machine learning model on each bootstrap copy and calculate the feature importance measure for each input feature. The black error bars in Figure 11 show the resulting 95% bootstrap confidence intervals (DiCiccio & Efron, 1996). For computational efficiency, we fit the machine learning model on each bootstrap sample using the tuning parameter configuration obtained in Section 5.2.2. The x -axis represents the feature importance in percentages, indicating the relative contribution of each feature to the predictive model. The six features with the highest feature importance are all associated with temperature. Additionally, based on the bootstrap confidence intervals, these features consistently exhibit the highest feature importance across the bootstrapped datasets. Among the top three features, we find `w_avg_Tmin_anom_11`, `w_avg_T.ind95`, and `w_avg_T.ind5_11` which denote the lagged weekly average of the daily minimum temperature anomalies, the weekly average of the daily hot day index, and the lagged weekly average of the daily cold-day index, respectively. In contrast, features related to weather factors such as `Wind`, `Hum`, and `Rain` demonstrate limited importance in the model, as they do not rank among the top 10 predictors. This is in line with earlier studies such as Braga et al. (2002) and Alberdi et al. (1998).

²²To create a non-parametric bootstrap copy of the training data, we randomly sample observations with replacement from the training data.

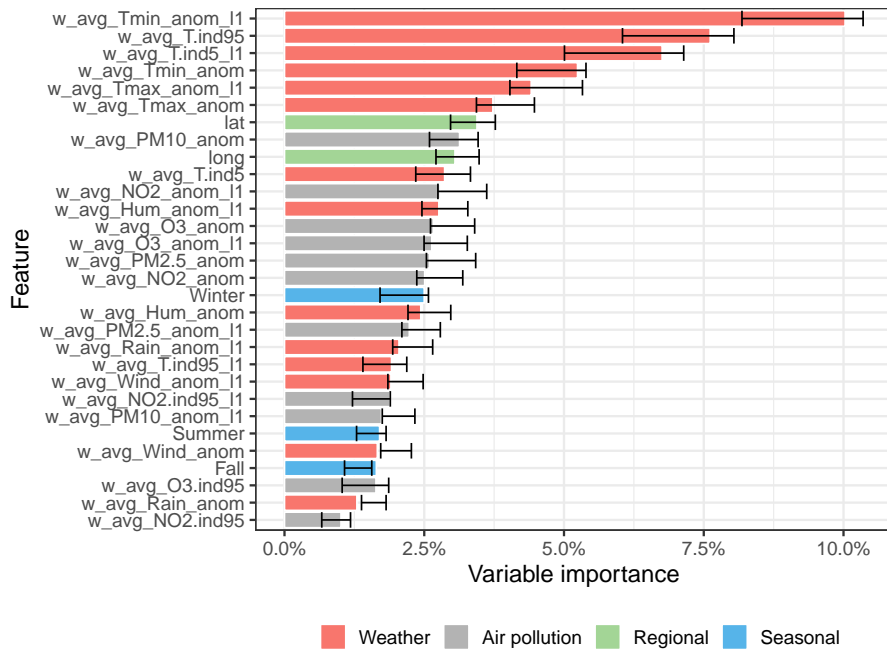


Figure 11: The features in the XGBoost model with a feature importance exceeding 1%. The feature importance of the features related to weather are visualized in red, air pollution in black, the NUTS 3 region in green, and the season in blue. Furthermore, the black error bars denote the 95% non-parametric bootstrap confidence interval for each feature based on 1 000 bootstrap samples of the training data.

ALE main effects. Figure 12 shows the ALE main effects for the features with an importance surpassing 1%. Features with lower importance in the machine learning model yield less reliable ALE main effects and we, consequently, exclude these from the illustration. Additionally, we show the 95% point-wise bootstrap confidence interval of the ALE main effect of each feature based on the fit constructed on each of the 1 000 bootstrap copies of the training data.

In Figure 12a, we observe an increasing trend in the ALE main effects corresponding to the four extreme temperature indices. We estimate that higher weekly averages of the daily hot or cold day indices, potentially lagged by one week, correspond to substantially higher excess deaths relative to the baseline. In accordance with the bootstrap-generated confidence intervals, these features have a statistically significant impact on the model’s predictions. In Figure 12b, we show the ALE main effect for the four temperature anomalies. The effect is the strongest and most significant for the feature `w_avg_Tmin.anom_11`. When the lagged weekly average of the daily minimum temperature anomalies is higher, the ALE main effect is lower, leading to a mortality deficit relative to the baseline on average. This effect might vary substantially from season to season. However, such an interaction effect can not be captured through ALE main effects. In Figure 12c, we illustrate the ALE main effects of the (lagged) weekly average of the daily humidity, precipitation, and wind speed anomalies. To a smaller extent, lower-than-baseline humidity levels from the previous week lead to more excess deaths compared to the effect of higher-than-baseline humidity levels, while higher precipitation levels from the previous week have the opposite effect. The other ALE main effects do not show any strong variation across the feature levels and their point-wise bootstrap confidence intervals contain or are close to zero. For the weekly averages of the extreme air pollution indices in Figure 12d, we also see, to a lesser extent, an increasing pattern in the ALE main effect. These ALE main effects are statistically significant as they do not encompass the value zero. Finally, in Figure 12e,

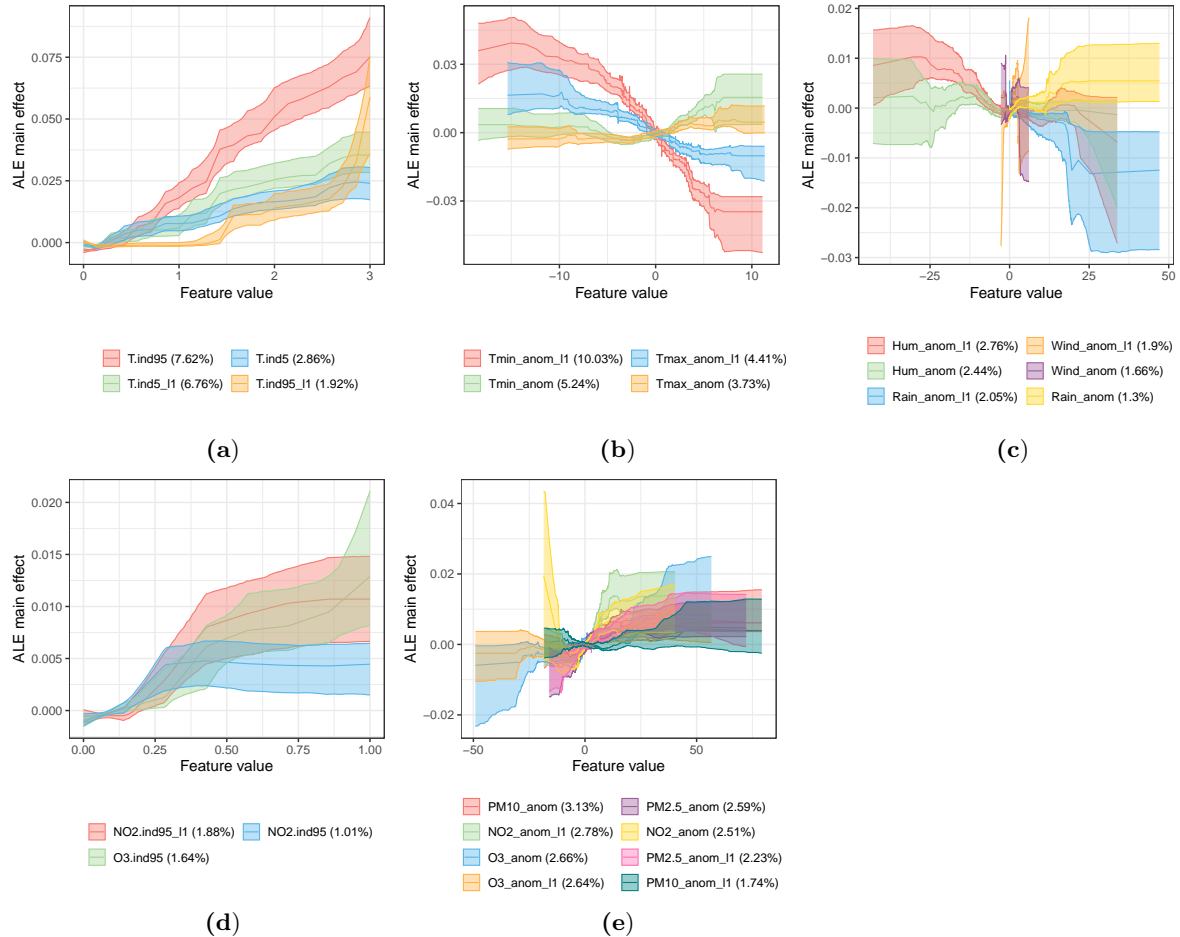


Figure 12: The ALE main effects for features whose feature importance exceeds 1%, denoted within parentheses in each panel’s legend. To enhance visualization, the prefix `w_avg_` was removed from the feature names in the legend. We furthermore present the 95% point-wise confidence interval based on 1000 bootstrap samples of the training data. The different panels display the ALE main effects of the extreme temperature indices (a), temperature anomalies (b), weather anomalies including humidity, wind speed, and rainfall (c), extreme air pollution indices (d), and air pollution anomalies (e).

most of the bootstrap confidence intervals of the ALE main effects stay close to zero, indicating that variations in the air pollution levels do not have a strong impact on excess deaths in the short term. However, for the feature `w_avg_no2_anom_11`, we observe that high lagged nitrogen dioxide levels above the baseline have a slightly, but significant, higher impact on excess deaths relative to low lagged nitrogen dioxide levels. We conclude that the (lagged) hot- and cold-week index features have the most substantial impact on excess mortality.

ALE regional effects. We examine regional differences in how environmental factors impact deviations from the mortality baseline. To achieve this, we re-compute the ALE main effect of a specific feature by restricting the training data to region r . Figures 13a and 13b visualize the results for the hot and lagged cold-week index respectively, at a value of 1.5, see Equation (5.3). Figure 13c shows the ALE regional effect of the feature `w_avg_NO2_anom_11`, i.e., the lagged weekly average of the daily NO_2 anomalies, at a value of $20 \mu\text{g}/\text{m}^3$. This corresponds to the situation wherein the daily NO_2 baseline concentrations are surpassed by $20 \mu\text{g}/\text{m}^3$ on average throughout the previous week.

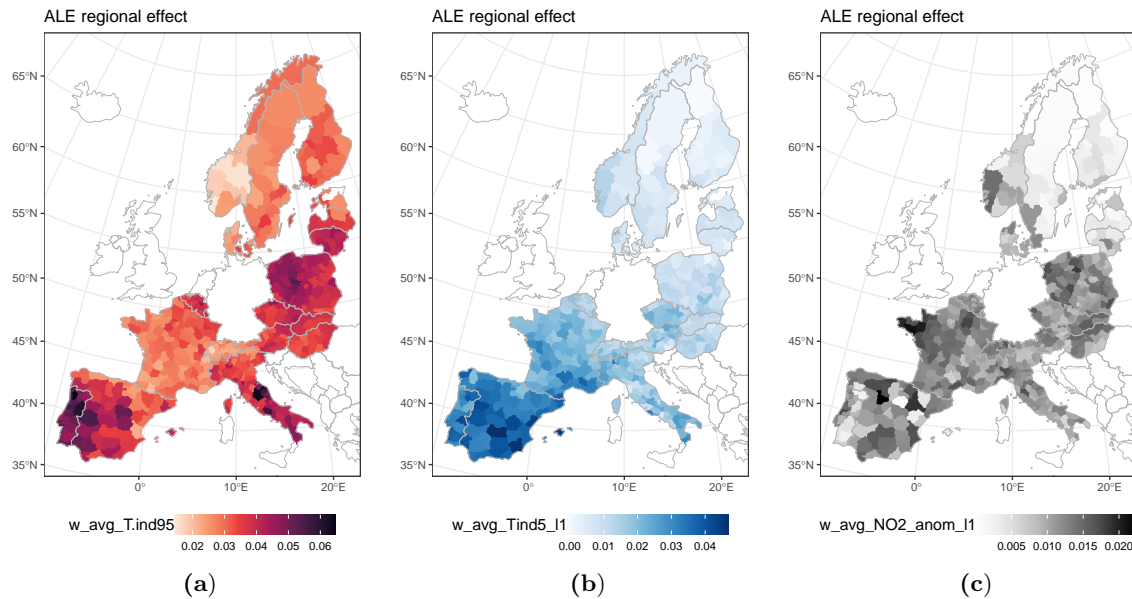


Figure 13: ALE regional effect of the features w_avg_Tind95 (a), $w_avg_Tind5_11$ (b), and $w_avg_NO2_anom_11$ (c) fitted on the training data restricted to each region and visualized at the values 1.5 , 1.5 , and $20 \mu\text{g}/\text{m}^3$ respectively.

We observe that the hot-week index exhibits the most pronounced effect in the southern NUTS 3 regions of Spain, Portugal, Italy, and certain Eastern European countries. Conversely, northern regions appear less impacted by high temperatures. The cold-week indicator follows a somewhat comparable pattern. In the right panel, no clear geographical pattern emerges for the weekly average of last week's daily nitrogen dioxide anomalies, except for nearly zero ALE values in northern NUTS 3 regions.

Figure 14 illustrates the regional ALE effects for the NUTS 3 regions of Barcelona, Milano, and Stockholm for the same features shown in Figure 13: w_avg_Tind95 , $w_avg_Tind5_11$, and $w_avg_NO2_anom_11$. Figure 14a shows a similar marginal impact of the hot-week index on deviations from the mortality baseline across the three considered regions, with a slightly lower observed impact in Stockholm at values for the hot-week index between 1 and 2. This could explain the behaviour in Figure 13a. Figure 14b indicates that the marginal impact of the lagged cold-week index on mortality deviations from the baseline is clearly lower in Stockholm, and clearly higher in Barcelona. This implies that individuals in Stockholm may tolerate extreme cold temperatures better. For the lagged nitrogen dioxide anomalies in Figure 14c, we see a similar marginal impact across the three considered regions.

ALE interaction effects. Using the method outlined in Section 4.3, we calculate the ALE interaction effect of the feature $w_avg_T.ind95$ with three other features: $w_avg_Tind95_11$, $w_avg_PM10_anom$, and $w_avg_Tmax_anom$. Figure 15a illustrates that elevated levels of the hot-week index for both the current and preceding week have a larger impact on excess mortality. However, when the previous week is hot while the current week is not, we observe the opposite effect. This is an indication of harvesting, as further investigated in Section 5.3.3. Moreover, Figure 15b shows that heightened PM10 values in combination with a hot week lead to higher excess mortality. Lastly, Figure 15c indicates that when the hot-week indicator is high and maximum temperatures significantly exceed their baseline, a higher impact is observed.

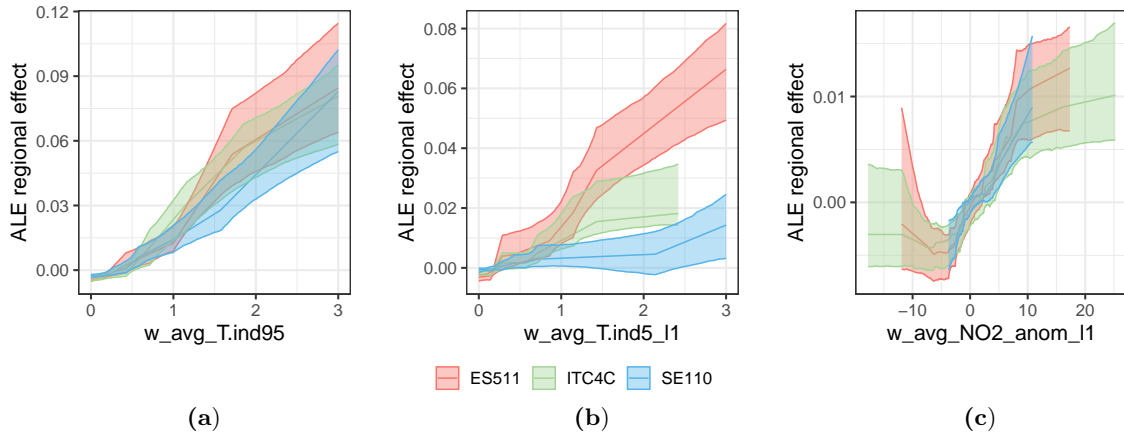


Figure 14: ALE regional effect in the NUTS 3 regions of Barcelona (red), Milano (green), and Stockholm (blue) for the features $w_{avg_T.ind95}$ (a), $w_{avg_T.ind5_11}$ (b), and $w_{avg_NO2.anom_11}$ (c) fitted on the training data restricted to region r . We show a point-wise confidence interval based on 1 000 bootstrap samples of the training data.

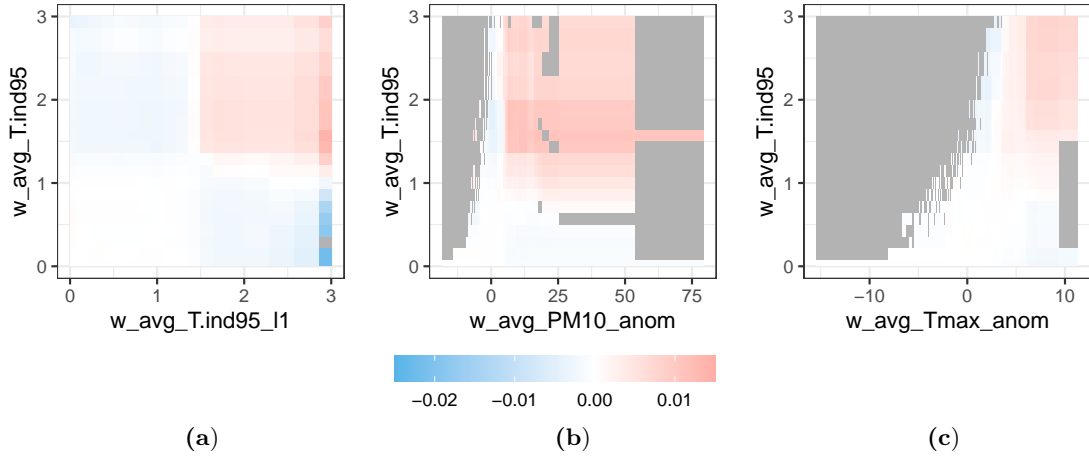


Figure 15: ALE interaction effects between the feature $w_{avg_T.ind95}$ and $w_{avg_T.ind95_11}$ (a), $w_{avg_PM10.anom}$ (b), and $w_{avg_Tmax.anom}$ (c). The grey squares indicate that there is no data available.

5.3.3 Harvesting effects

Harvesting effects occur when, for example, environmental related excess mortality in the previous week leads to a mortality deficit in the current week (Schwartz, 2001). We first conduct an exploratory analysis to empirically identify potential harvesting effects within our training data spanning from 2013 to 2019, across all considered NUTS 3 regions. We then assess if we observe similar effects using the predictions obtained from the machine learning model, calibrated in Section 5.2.2.

To quantify the difference in observed or estimated deaths relative to the mortality baseline for a specific week w in year t and region r , we calculate the excess death proportion or the so-called ‘P-score’ (Msemburi et al., 2023; Schöley, 2021), defined as:

$$EDP_{t,w}^{(r)} = \frac{d_{t,w}^{(r)} - \hat{b}_{t,w}^{(r)}}{\hat{b}_{t,w}^{(r)}}, \quad \widehat{EDP}_{t,w}^{(r)} = \frac{\hat{d}_{t,w}^{(r)} - \hat{b}_{t,w}^{(r)}}{\hat{b}_{t,w}^{(r)}},$$

for $t \in \mathcal{T}$, $w \in \mathcal{W}_t$, and $r \in \mathcal{R}$. Furthermore, $d_{t,w}^{(r)}$, $\hat{b}_{t,w}^{(r)}$, and $\hat{d}_{t,w}^{(r)}$ represent, respectively, the observed deaths, the deaths estimated by the baseline mortality model (see Equation (3.3)), and the deaths estimated by the machine learning model (see Equation (3.4)). Next, we consider a specific feature $\mathbf{f}_{t,w}$ from Table 3 in week w of year t and denote its lagged version as $\mathbf{f_11}_{t,w} := \mathbf{f}_{t,w-1}$.²³ We then partition the domain of this feature into B equal intervals denoted as $[a_0, a_1]$, $[a_1, a_2]$, ..., $[a_{B-1}, a_B]$, where a_0 and a_B denote the minimum and maximum values observed in the training data. This creates a two-dimensional grid for the interaction $\mathbf{f} \times \mathbf{f_11}$. We calculate the average relative change in observed deaths with respect to the mortality baseline in each grid cell $[a_{i-1}, a_i] \times [a_{j-1}, a_j]$, for $i, j \in \{1, 2, \dots, B\}$, as:

$$\mathcal{D}_{\mathbf{f}}^{(i,j)} = \frac{1}{n_{i,j}} \sum_{r \in \mathcal{R}} \sum_{t \in \mathcal{T}} \sum_{w \in \mathcal{W}_t} \text{EDP}_{t,w}^{(r)} \cdot \mathbb{1} \left\{ \mathbf{f_11}_{t,w}^{(r)} \in [a_{i-1}, a_i] \wedge \mathbf{f}_{t,w}^{(r)} \in [a_{j-1}, a_j] \right\}, \quad (5.5)$$

where $\mathbb{1}\{\cdot\}$ is an indicator function, equaling one when the argument holds true and zero otherwise, and $n_{i,j}$ denotes the number of training observations falling inside the grid cell $[a_{i-1}, a_i] \times [a_{j-1}, a_j]$. We define $\hat{\mathcal{D}}_{\mathbf{f}}^{(i,j)}$ as the average relative change in estimated deaths from the XGBoost model with respect to the mortality baseline, and calculate it by using $\widehat{\text{EDP}}_{t,w}^{(r)}$ in Equation (5.5). Comparing the observed and estimated relative differences provides insights into how effectively the XGBoost model captures interaction effects present in the training data.

Figure 16 illustrates the results of the aforementioned method for the four extreme environmental indices `w_avg_T.ind95`, `w_avg_T.ind5`, `w_avg_N02.ind95`, and `w_avg_O3.ind95`. The term “harvesting effect” is employed when, e.g., high temperatures in the current week lead to excess deaths, yet the subsequent week with normal temperatures results in a mortality deficit compared to the baseline. This concept applies to any weather or air pollution factor. Based on Figure 16, the harvesting effect appears most pronounced for the hot-week index, see the green color in the bottom right corner of Figure 16a. This suggests that following a very hot week succeeded by a week of normal temperatures, observed death counts are lower on average by approximately 5% relative to the baseline (more green colors). Conversely, Figure 16b reveals that the cold-week index does not exhibit a harvesting effect in our observations, since we even observe additional excess deaths one week after a cold week, regardless of the temperature. Moreover, no harvesting effect is detected for the weekly extreme NO₂ index (see Figure 16c), while Figure 16d shows a slight harvesting effect for the weekly extreme ozone index. We also observe that two consecutive weeks with high air pollution levels of NO₂ or O₃ result in higher excess deaths, indicating the presence of interaction effects in the data. Lastly, we observe a close correspondence between the observed and estimated excess death proportions, indicating that the XGBoost model effectively captures the interaction effects present in the data.

5.4 Temporal and spatial aggregation

While detailed mortality insights at a fine-grained regional and weekly level are valuable for, e.g., swiftly detecting signals of excess mortality, many applications in healthcare and life insurance, particularly those involving policy making and long-term risk assessment, require mortality statistics aggregated at an annual or national level. In this section, we evaluate the advantages of initially crafting a mortality model that is region-specific, weekly, and incorporates weather and air pollution factors, followed by aggregating observations or estimates over the temporal and spatial dimensions of the data.

²³Note that $\mathbf{f}_{t,0}$ represent $\mathbf{f}_{t-1,53}$ (leap year) or $\mathbf{f}_{t-1,52}$ (non-leap year)

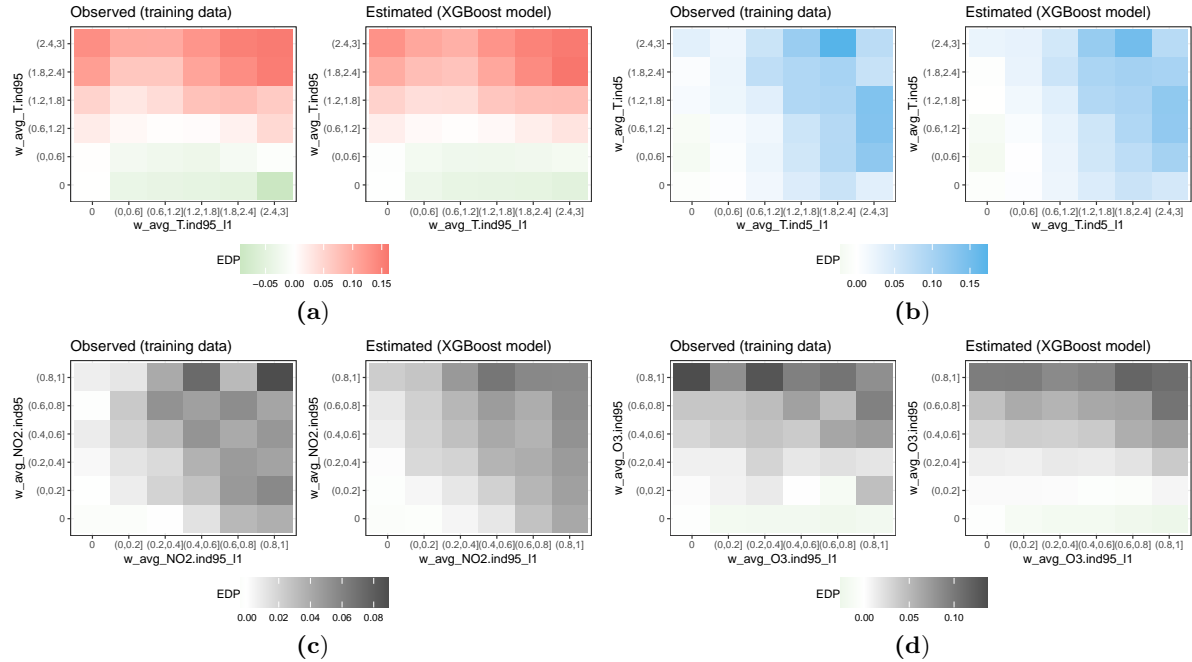


Figure 16: The average relative difference in observed and estimated deaths relative to the weekly mortality baseline model, defined in grid cells of the feature and its lagged version for $w_{avg_T.ind95}$ (a), $w_{avg_T.ind5}$ (b), $w_{avg_NO2.ind95}$ (c), and $w_{avg_O3.ind95}$ (d).

Temporal aggregation. At NUTS 3 level we aggregate the observed and estimated weekly mortality statistics to an annual time scale as follows:

$$d_t^{(r)} = \sum_{w \in \mathcal{W}_t} d_{t,w}^{(r)}, \quad \hat{b}_t^{(r)} = \sum_{w \in \mathcal{W}_t} \hat{b}_{t,w}^{(r)}, \quad \hat{d}_t^{(r)} = \sum_{w \in \mathcal{W}_t} \hat{d}_{t,w}^{(r)}, \quad E_{t,w}^{(r)} = \sum_{w \in \mathcal{W}_t} E_{t,w}^{(r)},$$

for $t \in \mathcal{T}$ and $r \in \mathcal{R}$. Using mortality data at annual level, a simple benchmark approach is to estimate the annual number of deaths using a Poisson GLM, i.e., we assume:

$$D_t^{(r)} \sim \text{Poisson} \left(E_t^{(r)} \cdot \mu_t^{(r)} \right), \quad (5.6)$$

where the annual force of mortality $\mu_t^{(r)}$ for each region r equals:

$$\log \mu_t^{(r)} = \beta_0^{(r)} + \beta_1^{(r)} t.$$

Figure 17 illustrates the observed deaths (grey dots) alongside the estimated annual death counts derived from the benchmark Poisson GLM in Equation (5.6) (green line). The figure also plots the estimated weekly deaths aggregated to an annual time scale as obtained with the weekly Serfling-type baseline model in Equation (3.1) (red line) and the XGBoost model incorporating environmental features in Equation (3.4) (blue line). We observe a better in-sample fit for the NUTS 3 regions of Barcelona and Milano, indicating the usefulness at annual level of adding region-specific environmental factors into a weekly mortality model. For Stockholm, the improvement is less pronounced as we see a slightly worse in-sample fit for the years 2014-2016, but a slightly better in-sample fit for the years 2018-2019. Appendix D.4 outlines a statistical in-sample comparison between the three considered models by means of the Poisson deviance. We find that approximately 80% of the regions favour the XGBoost model.

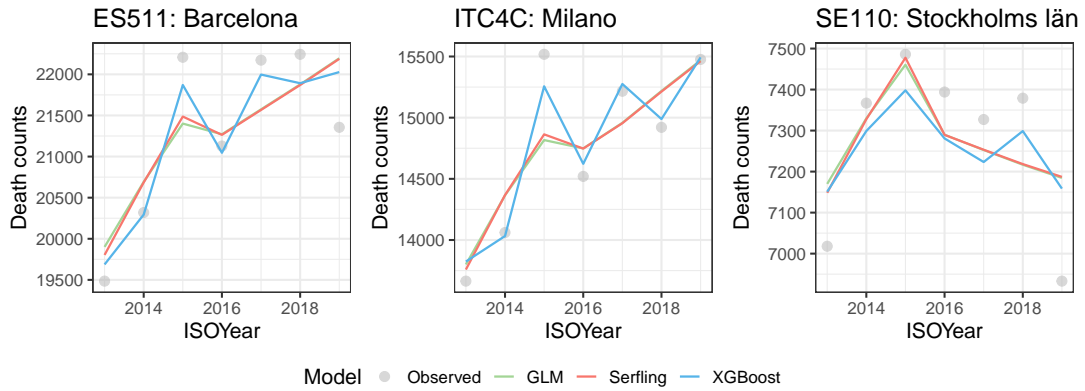


Figure 17: Observed annual death counts (grey dots), and the estimated annual death counts from the Poisson GLM (green line), the weekly Serfling-type baseline model (red line), and the XGBoost model including environmental features (blue line). We display the results for the NUTS 3 regions Barcelona (middle), Milano (middle), and Stockholm (right).

Spatial aggregation. We also aggregate the region-specific, annual observed and estimated death counts to country-level. Hereto, let \mathfrak{C} be the set of countries considered in this case study and \mathcal{R}_c the set of NUTS 3 regions that belong to country $c \in \mathfrak{C}$. We define:

$$d_t^{(c)} = \sum_{r \in \mathcal{R}_c} d_t^{(r)}, \quad \hat{b}_t^{(c)} = \sum_{r \in \mathcal{R}_c} \hat{b}_t^{(r)}, \quad \hat{d}_t^{(c)} = \sum_{r \in \mathcal{R}_c} \hat{d}_t^{(r)}, \quad E_t^{(c)} = \sum_{r \in \mathcal{R}_c} E_t^{(r)},$$

for every $c \in \mathfrak{C}$. We aggregate the estimated death counts from the weekly mortality baseline and the machine learning model and compare these with the estimated death counts from a GLM using a Poisson assumption for the annual number of deaths in each country $c \in \mathfrak{C}$:

$$D_t^{(c)} \sim \text{Poisson} \left(E_t^{(c)} \cdot \mu_t^{(c)} \right), \quad (5.7)$$

where the annual force of mortality for each country c follows:

$$\log \mu_t^{(c)} = \beta_0^{(c)} + \beta_1^{(c)} t.$$

Figure 17 displays the observed death counts (grey dots) alongside the estimated annual, country-specific death counts obtained from the Poisson GLM in Equation (5.7) (green line), and the estimated weekly deaths aggregated to a country-level and annual time scale as derived from the weekly Serfling baseline model (red line), and the machine learning model (blue line). Consistent with the regional findings, the XGBoost model is the preferred model for Spain and Italy, showcasing the usefulness of environmental factors. When evaluating the in-sample Poisson deviance in each considered country for each of the three models, we find that the XGBoost model including environmental features outperforms the Serfling and simple Poisson GLM in 18 out of the 20 countries. The GLM performs best in Liechtenstein, while the Serfling model performs best in Finland.

5.5 Back-testing

We back-test the proposed weekly mortality modeling framework by projecting the death counts in the European NUTS 3 regions for the year 2019. Hereto, we recalibrate the weekly mortality model on weekly mortality and environmental data for the years 2013 to 2018.

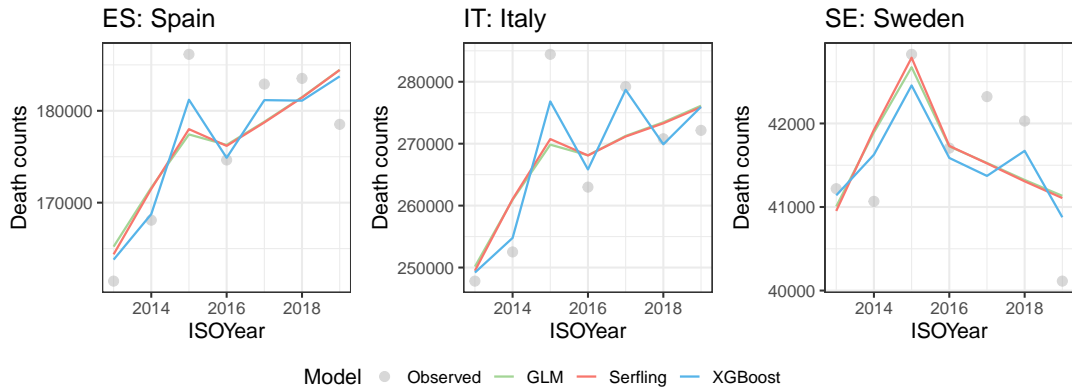


Figure 18: Observed annual death counts (grey dots), and the estimated country-specific annual death counts from the Poisson GLM (green line), the weekly Serfling-type baseline model (red line), and the XGBoost model including environmental features (blue line). We display the results for the countries Spain (left), Italy (middle), and Sweden (right).

We first calibrate the weekly mortality baseline model, as presented in Equations (3.1) and (3.2), using the weekly death counts for the years 2013-2018. This calibration follows the strategy outlined in Section 4.1. For computational purposes, we adopt the same penalty parameter values as obtained during the calibration process of Section 5.2.1 using death counts from 2013 to 2019. Nevertheless, we anticipate that this choice will only have a minor impact on the calibrated baseline death counts. We denote the resulting fitted baseline structure as $\hat{\mu}_{t,w}^{(r)}$, for week w in year t and region r . Subsequently, we use this calibrated baseline model to forecast the death counts in the year 2019 as follows:

$$\hat{b}_{2019,w}^{(r)} = E_{2019,w} \cdot \exp\left(\left(\hat{\beta}^{(r)}\right)^T z_{2019,w}\right),$$

with $\hat{\beta}$ the estimated parameter vector obtained from the calibration over the years 2013-2018 and $z_{2019,w}$ the vector consisting of the covariates in the baseline model evaluated in the year 2019, see Section 4.1.

Next, we continue with the environmental data spanning the years 2013 to 2018, as outlined in Section 2.2. We create environmental anomalies and extreme environmental indices following the feature engineering process detailed in Section 5.1. These engineered features serve as input in the machine learning model, enabling us to estimate the excess or deficit deaths relative to the calibrated baseline for the aforementioned years. During the calibration phase of the machine learning model, we solely focus on the tuning parameters related to the maximum tree depth and the number of trees and maintain the remaining parameters at the values determined in Section 5.2.2. Using the calibrated environmental baseline models established from data spanning 2013 to 2018, we then proceed with the feature engineering process using the registered observations for the year 2019. Subsequently, the resulting 2019 environmental features are used as inputs for the calibrated machine learning model to forecast death counts across the European NUTS 3 regions for the year 2019.

Figure 19 illustrates the outcomes for the NUTS 3 regions of Barcelona, Milano, Stockholm, Lisboa, Varese, and Rhône. The results indicate a clear advantage of the machine learning model (blue line) over the baseline model (red line) in Milano, Lisboa, and Varese, see Figures 19b, 19d, and 19e. Specifically, the XGBoost model correctly predicts higher-than-baseline deaths in the first weeks of 2019 and during the summer of 2019 in Milano and Varese. However, in Barcelona, Stockholm and Rhône, in Figures 19a, 19c, and 19f, we conclude that the calibrated baseline

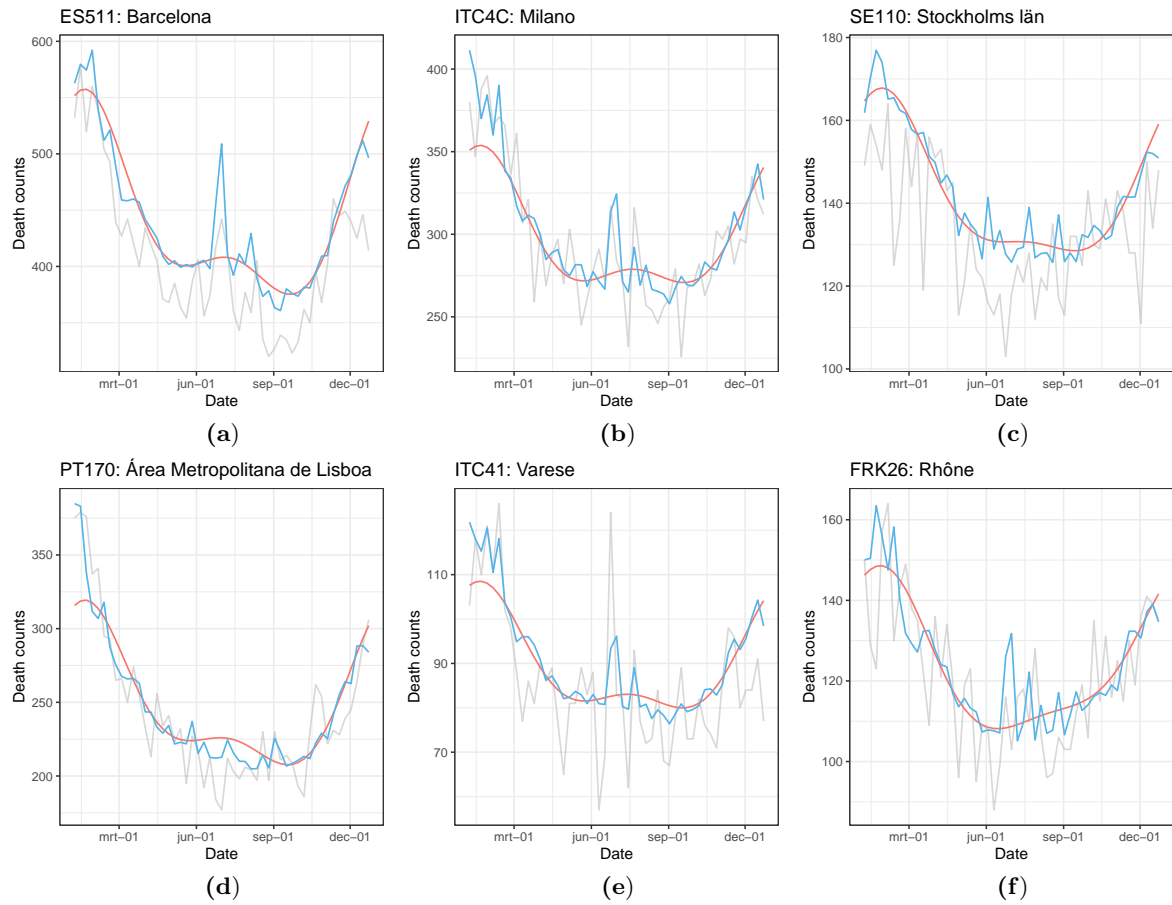


Figure 19: The observed and projected death counts for the year 2019 in the NUTS 3 regions of Barcelona (a), Milano (b), Stockholm (c), Lisboa (d), Varese (e), and Rhône (f). The observed death counts are visualized in grey and the death counts as obtained from the weekly baseline mortality model and the XGBoost model in red and blue, respectively.

model consistently overestimates the observed deaths in 2019 and henceforth fails to accurately capture the region-specific seasonal mortality trend. Nevertheless, the machine learning model fulfills its task as the pattern and spikes, present in the observed and estimated death counts from the XGBoost model, largely coincide. This is particularly true for Barcelona and Rhône, while in the region around Stockholm, it is less pronounced. However, this aligns with our earlier observation that the northern regions appear to be less impacted by extreme environmental levels, see Figure 13 for example. It is worth noting that since the back-test relies on data from only a single year, we refrain from drawing further conclusions.

To compare the performance of our weekly mortality model, integrating environmental features, across all considered European NUTS 3 regions, Figure D.3b in Appendix D.5 displays the relative change in the Poisson deviance of the XGBoost model relative to the one of the weekly baseline mortality model. We find that, based on the one year-prediction results, adding environmental features is beneficial in about 55% of the NUTS 3 regions. Northern regions seem to experience little benefit from the integration of environmental features, while southern regions generally benefit more.

6 Conclusions

This paper proposes a comprehensive framework for integrating environmental features, related to weather and air pollution factors, into a weekly mortality model using fine-grained, open source data. Building upon the established weekly Serfling-type mortality model, we enhance this so-called weekly baseline model by incorporating environmental anomalies and extreme environmental indices through a machine learning approach to explain short-term deviations from the mortality baseline.

Through a case study spanning over 550 NUTS 3 regions in 20 European countries among individuals aged 65 and older, we find clear short-term associations between temperature anomalies and extreme indices and deviations from the mortality baseline. While some air pollution features also contribute significantly, other weather-related variables such as humidity, rainfall, and wind speed are only of minor importance. To address the correlation among the environmental features, we employ Accumulated Local Effect plots to investigate the short-term marginal impact of the environmental features as well as their interactions on deviations from the mortality baseline, for individuals aged 65 and older. We hereby find that the hot-week index, indicating the frequency of days surpassing the 95% temperature threshold within a week, exhibits the most pronounced effect on excess deaths. Moreover, regional disparities emerge, with southern regions estimated to have higher excess deaths associated with both hot and cold week indices compared to northern regions. Our analysis further unveils a harvesting effect for the hot-week index, suggesting a mortality deficit following hot preceding weeks. Next, we demonstrate the added contribution of environmental factors when aggregating the estimated weekly mortality rates from the machine learning model on an annual, country-level basis. Additionally, through back-testing, we validate the model's ability to explain excess deaths relative to the baseline in an out-of-sample year.

The proposed modeling framework can provide a valuable tool for evaluating the potential impact of specific environmental scenarios on mortality outcomes. By generating region-specific environmental scenarios for temperature, weather factors, and air pollution concentrations, we can assess the associated risks of excess deaths across different regions. Through feature engineering and utilization of machine learning techniques like XGBoost, we will then be able to estimate risk ratios, representing multipliers that augment or diminish the baseline number of deaths. Such findings can inform policymakers about the potential health implications of various environmental changes, guiding proactive measures to mitigate risks and protect vulnerable populations. However, when estimating mortality risk using environmental scenario projections, incorporating the benefits and costs of climate change adaptation becomes an additional challenge, as demonstrated by [Carleton et al. \(2022\)](#).

In future research, it will be valuable to conduct a similar study on cause-of-death mortality data to investigate how environmental factors influence excess deaths across various causes. Additionally, we can explore the robustness of our proposed weekly mortality modeling framework by exploring alternative weekly mortality models as baselines, as suggested by [Schöley \(2021\)](#) and by using weather-station data instead of fine-grained gridded datasets from the Copernicus Climate Data Store and the Copernicus Atmospheric Monitoring Service.

Data and code availability statement

The datasets used in this paper are publicly available. We consulted the deaths by week, sex, 5-year age group and NUTS 3 region on Eurostat (<https://ec.europa.eu/eurostat/>

databrowser/view/demo_r_mweek3/, downloaded on January 20, 2024). We retrieved the weather-related variables from the Copernicus Climate Data Store (<https://cds.climate.copernicus.eu/>, downloaded on January 22, 2024) and the air pollution variables from the Copernicus atmospheric monitoring service (<https://ads.atmosphere.copernicus.eu/>, downloaded on January 22, 2024). The code used for the implementation and analysis of the case study presented in this paper is available on the following GitHub repository (<https://github.com/jensrobben/EnvVar-Mortality-Europe>). The code is written in R and can be accessed and downloaded for further reference and replication of the obtained results.

Funding statement

Katrien Antonio acknowledges funding from the FWO and F.R.S.-FNRS under the Excellence of Science (EOS) programme, project ASTeRISK (40007517). The FWO WOG network W001021N is acknowledged as well. Katrien Antonio acknowledges support from the Chair of Excellence on Digital Insurance And Long-term risk (DIALog) by CNP Assurances. This study is furthermore part of the research programme at the Research Centre for Longevity Risk. RCLR is a joint initiative of NN Group and the University of Amsterdam, with additional funding from the Dutch government's Public-Private Partnership (PPP) programme.

Conflict of interest disclosure

The authors declare no conflict of interest.

Appendices

A Methodological approaches in the epidemiological and medical literature: a literature review

In exploring the relationship between environmental factors and mortality statistics, various methodologies have been proposed in the epidemiological and medical literature.

Minimum mortality temperature bands. Keatinge et al. (2000) conduct an observational study to investigate heat-related mortalities across Europe. Hereto, they compute the daily death rates $m_{65-74,t}^{(r)}$ of individuals aged 65-74 at time t per million population for several regions r including North Finland, South Finland, Baden-Württemberg, Netherlands, London, North Italy, and Athens from 1988 to 1992. They then retrieve region-specific, daily mean temperatures from the Royal Meteorological Office and calculate the average death rate per million population across successive temperature bands of 3°C , each separated by 0.1°C . Hereto, let T° be any temperature in degrees Celsius and define the set of time points at which the temperature T° is exceeded in region r :

$$\mathcal{S}_r(T^{\circ}) = \left\{ t \mid T^{\circ} \leq \text{Tavg}_t^{(r)} < T^{\circ} + 3^{\circ}\text{C} \right\},$$

with $\text{Tavg}_t^{(r)}$ the region-specific daily mean temperature at time t (in daily date format). The average region-specific death rate per million population in temperature band $[T^\circ, T^\circ + 3^\circ\text{C}]$ is then defined as:

$$\bar{m}_{65-74}^{(r,T^\circ)} = \frac{1}{|\mathcal{S}_r(T^\circ)|} \sum_{t \in \mathcal{S}(T^\circ)} m_{65-74,t}^{(r)},$$

Subsequently, they identify the temperature band with the lowest death rate in each region, i.e., $[T^{(\star,r)}, T^{(\star,r)} + 3^\circ\text{C}]$, also called the region-specific minimum mortality temperature (band), and find that these bands are significantly higher in regions with hot summer temperatures, e.g., Athens with $[22.7^\circ\text{C}, 25.7^\circ\text{C}]$, compared to regions with cold summer temperatures, e.g., north Finland with $[14.3^\circ\text{C}, 17.3^\circ\text{C}]$. They then calculate the annual heat-related mortality in each region r as the average number of days the minimum mortality temperature band was exceeded in a year, multiplied by the mean difference of the daily death rates per million population at temperatures above the minimum mortality temperature band with the daily death rate per million population within this band. These differences are calculated as:

$$m_{65-74,t}^{(r)} - \bar{m}_{65-74}^{(r,T^\circ)},$$

for time points t at which the average temperature $\text{Tavg}_t^{(r)}$ exceeds $T^{(\star,r)} + 3^\circ\text{C}$. They find that regions with hot summers did not exhibit significantly higher annual heat-related mortality compared to colder regions. They conclude that European populations have effectively acclimated to average summer temperatures, and can be expected to adapt to the predicted global warming, see [Hulme and Jenkins \(1998\)](#), with only a small increase in heat-related mortality. However, such an approach typically overlooks the non-linear relationship between temperature and the (daily) mortality statistics.

Time series models. Yet another strand in the literature relies on time series regression models. Here, researchers typically assume an overdispersed Poisson distribution for the daily death counts, with as an exploratory variable the observed daily temperature values or daily measurements of a particular air pollutant, alongside other time-varying confounding factors ([Armstrong, 2006](#)). As an example, the structure of such a time series regression model, with the daily average temperature Tavg as the explanatory variable of interest, is typically represented as:

$$\log \mathbb{E} [D_t^{(r)}] = \alpha^{(r)} + f \left(\text{Tavg}_t^{(r)} \mid \boldsymbol{\beta}^{(r)} \right) + (\text{confounding covariates})_t^{(r)} + (\text{smooth function of time})_t^{(r)}, \quad (\text{A.1})$$

where $D_t^{(r)}$ is the death count random variable from a specific region r at time t and α denotes the intercept term. Furthermore $f^{(r)}(\text{Tavg}_t^{(r)} \mid \boldsymbol{\beta})$ denotes the function capturing the relationship between the region-specific daily average temperature and the daily death counts at time t and region r , also known as the temperature-mortality association, parametrized through a vector $\boldsymbol{\beta}$. Examples of confounding factors include daily measurements of air pollution or other weather-related covariates, such as humidity, rainfall, and wind speed, that may influence the daily death counts. The smooth function of time is incorporated into the model to accommodate for seasonal effects and demographic shifts ([Armstrong, 2006](#)). While earlier studies such as [The Eurowinter Group \(1997\)](#) and [Lovett et al. \(1986\)](#) favoured Poisson regression models with a linear functional form for modeling the temperature-mortality association, later research by [Braga et al. \(2002\)](#) suggests a more nuanced U-, V-, or J-shaped association between daily death counts and daily temperature values, necessitating a non-linear functional

form. Hereto, [Armstrong \(2006\)](#) mentions that natural cubic splines are typically used for modeling the temperature-mortality association.

Studies by [Braga et al. \(2001\)](#) and [Pattenden et al. \(2003\)](#) reveal that the impact of a cold spell on mortality may persist for a week or longer, while the effects of heat are more immediate. Additionally, [Verhoeff et al. \(1996\)](#) applies time series Poisson regression models to find a positive correlation between ozone levels and daily mortality in Amsterdam, with effects persisting for up to two days. Ozone is a significant contributor to smog at ground level and can harm the respiratory system ([Mudway & Kelly, 2000](#)). [Sunyer et al. \(1996\)](#) show similar findings in Barcelona for other air pollutants such as sulphur and nitrogen dioxide. Sulphur dioxide mainly originates from fossil fuel burnings and irritates the respiratory tract and eyes, posing heightened risks to asthmatic patients, while nitrogen dioxide is a toxic gas that induces respiratory issues and can lead to a reduced lung function ([Devalia et al., 1994](#)). These studies indicate that the effects of a particular event, such as a cold spell, heat wave, or elevated air pollution levels, may extend beyond the period in which it occurs, and possibly exhibit delayed impacts over time.

Distributed lag models. To adequately address such delayed effects, researchers have proposed distributed lag models (DLMs). A DLM is a linear, additive regression model for time series data that predicts the current values of a dependent variable using both current and past (lagged) values of an explanatory variable. [Almon \(1965\)](#) initially proposes the DLM to model quarterly capital expenditures in manufacturing industries, but the framework has been applied in other fields such as epidemiology, as highlighted by [Pope and Schwartz \(1996\)](#). [Schwartz \(2000\)](#) further refines the DLM and applies it to a case study to estimate a biologically plausible lag structure between daily air pollution levels and daily deaths across ten cities in the United States (US). Additionally, [Braga et al. \(2001\)](#) examine the delayed impact of temperature and humidity on overall daily mortality in 12 US cities. In scenarios where the daily average temperature serves as the explanatory variable of interest, the DLM's model specification is similar to the time series regression model of Equation (A.1), but with the following lagged functional form to model the temperature-mortality association:

$$f\left(\text{Tavg}_t^{(r)} \mid \boldsymbol{\beta}^{(r)}\right) = \sum_{l=0}^L \beta_l^{(r)} \cdot \text{Tavg}_{t-l}^{(r)}, \quad (\text{A.2})$$

where L is the maximum number of lags considered. To avoid collinearity issues, [Almon \(1965\)](#) and [Schwartz \(2000\)](#) suggest to constrain the parameters corresponding to the different lags. More specifically, they assume that the $\beta_l^{(r)}$'s, for $l = 0, 1, \dots, L$, follow a polynomial function with parameters $\eta_k^{(r)}$, for $k = 0, 1, \dots, v_L$:

$$\beta_l^{(r)} = \sum_{k=0}^{v_L} \eta_k^{(r)} l^k. \quad (\text{A.3})$$

Hence, the $\beta_l^{(r)}$'s are modelled as smooth functions using polynomial basis functions of the lag dimension.

To enhance modeling flexibility, [Zanobetti et al. \(2000\)](#) propose a comprehensive framework by combining DLMs with generalized additive models. Expanding on our example where the daily average temperature is used as explanatory variable of interest, they generalize the time series regression model in Equation (A.1) using the DLM structure in Equation (A.2) to:

$$\log \mathbb{E}\left[D_t^{(r)}\right] = \alpha^{(r)} + \left(\boldsymbol{\gamma}^{(r)}\right)^T \mathbf{z}_t^{(r)} + \sum_{i=1}^d g_i\left(s_{i,t}^{(r)}\right) + \sum_{l=0}^L \beta_l^{(r)} \cdot \text{Tavg}_{t-l}^{(r)}, \quad (\text{A.4})$$

where $\mathbf{z}_t^{(r)}$ denotes a set of region-specific confounding covariates modelled linearly through the region-specific parameter vector $\boldsymbol{\gamma}^{(r)}$, and $g_i(s_{i,t}^{(r)})$'s denote smooth functions of time or of confounding covariates in region r . The parameter vector $\boldsymbol{\beta}^{(r)}$ follows the polynomial function from Equation (A.3) to ensure smoothness along the lag dimension. Zanobetti et al. (2000) demonstrate the utility of their approach by modeling the association between lagged daily air pollution levels and daily death counts in Milano. Due to the incorporation of lagged effects, DLMs are valuable in identifying harvesting effects, where particular events, such as extreme temperatures, disproportionately impact vulnerable individuals. This precipitates events like deaths, leading to short-term higher mortality rates relative to the baseline (Schwartz, 2001). Afterwards, the mortality rates are lower than expected. This phenomenon is known as harvesting (Zanobetti et al., 2000). In conclusion, the main advantage of DLMs lies in their ability to incorporate a detailed representation of the time-course of the temperature-mortality or air pollution-mortality relationship and provide information about the overall effect even in the presence of delayed contributions or harvesting.

Distributed lag non-linear models. While the extension of Zanobetti et al. (2000) provides a more flexible approach, DLMs can only be used to model the lag structure of linear effects, see Equation (A.4). As such, their proposed model structure exhibits limitations in representing the lag structure of non-linear relationships. Therefore, Gasparrini et al. (2010) introduce Distributed Lag Non-linear Models (DLNMs), a versatile family of models capable of describing non-linear effects along the predictor space and the lag dimension. Here, we select a set of $v_E + 1$ basis functions for the explanatory variable of interest, denoted as $b_j(\cdot)$, for $j = 0, 1, \dots, v_E$. Examples include polynomials or spline functions. The DLNM specification is similar to the generalized additive DLM shown in Equation (A.4). However, in this model, the lagged functional form of the explanatory variable is expressed as (Gasparrini et al., 2010):

$$f\left(\text{Tavg}_t^{(r)} \mid \boldsymbol{\beta}^{(r)}\right) = \sum_{l=0}^L \sum_{j=0}^{v_E} \beta_{j,l}^{(r)} \cdot b_j(\text{Tavg}_{t-l}^{(r)}). \quad (\text{A.5})$$

To address collinearity issues, similar constraints as in Equation (A.3) can be imposed:

$$\beta_{j,l}^{(r)} = \sum_{k=0}^{v_L} \eta_{j,k}^{(r)} l^k, \quad (\text{A.6})$$

for all $j = 0, 1, \dots, v_E$ and $l = 0, 1, \dots, L$. By utilizing the $v_E + 1$ basis functions for the explanatory variable, they ensure a smooth, non-linear relationship between temperature and daily death counts. Meanwhile, the constraints on $\beta_{j,l}^{(r)}$ using $v_L + 1$ polynomial basis functions guarantee a smooth delayed impact across consecutive lags. For interpretation purposes, we presented here a somewhat simplified representation of the DLNM. Gasparrini et al. (2010) extend the DLNM structure from Equation (A.5) by introducing a general set of basis functions for the lag dimension, rather than the polynomial basis functions used in Equation (A.6).

The application of DLNMs is widespread in the epidemiological literature, particularly to study the health impacts of air pollution and weather factors across multiple locations. In this setting, researchers typically adopt a two-stage analytical design. In the first stage, location-specific temperature-mortality or air pollution-mortality associations are estimated using time series regression models such as DLMs or DLNMs. These estimated location-specific relationships are entirely described by the basis functions $b_{j,l}(\cdot)$, the lag dimension, and the estimated parameters $\hat{\boldsymbol{\eta}}^{(r)} \in \mathbb{R}^{(v_E+1) \times (v_L+1)}$ in the DL(N)M structure, see e.g., Equation (A.5) and (A.6). The estimated parameters then form the response for a (multivariate) meta-analytical modeling

technique in the second stage (Gasparrini & Armstrong, 2013; Gasparrini et al., 2012). As such, meta-regression, a particular meta-analytical technique, groups and synthesizes results from different locations obtained from the first stage location-specific regression models while adjusting for region-specific covariate effects. More specifically, the estimated parameters from the DLNM of location r are grouped into a column vector of size $(v_E + 1) \times (v_L + 1)$, denoted as $\hat{\eta}^{(r)}$. Such a multivariate meta-regression model is defined as:

$$\hat{\eta}^{(r)} \sim \mathcal{N} \left(\mathbf{U}^{(r)} \boldsymbol{\zeta}, \mathbf{S}^{(r)} + \boldsymbol{\Psi} \right),$$

where $\mathbf{U}^{(r)}$ encompasses region-specific covariate effects, referred to as meta-variables. The matrices $\mathbf{S}^{(r)}$ and $\boldsymbol{\Psi}$ represent the within and between-location covariance matrices, respectively. The parameter vector $\boldsymbol{\zeta}$ describes the association between the meta-variables and the estimated parameters from the DLNM structure. Employing this two-stage approach, Gasparrini et al. (2015) conduct a systematic assessment of the impact of temperature on mortality across various countries in the world, revealing that on average 7.71% of the total daily death counts can be attributed to both heat and cold, see Gasparrini and Leone (2014) for the concept of attributable risk in the context of distributed lag models. Moreover, they find that cold temperatures exert a more significant impact on mortality than heat. Additionally, Gasparrini and Armstrong (2011) use a DLNM combined with meta-regression to examine the impact of heat waves on daily death counts. They find that the excess risk associated with heat waves in the United States could be largely attributed to the single, independent effects of daily high temperatures, with a slight additional effect observed in heat waves lasting more than four days. However, a multi-country, multi-community investigation using DLNMs and meta-analysis by Guo et al. (2017) reveals significant cumulative associations between heat waves and mortality across all countries, although the significance varies by community. Interestingly, they find that heat waves exhibit stronger associations with mortality in areas experiencing moderate cold and moderate hot temperatures compared to cold and hot areas.

B Weekly mortality baseline model: specification of the penalty matrix

Consider the following specification of the penalty matrix $\mathbf{S} = (s_{ij})_{i,j \in \mathcal{R}}$:

$$s_{ij} = \begin{cases} |\mathcal{N}_i| & \text{if } i = j \\ -1 & \text{if } i \neq j \text{ are neighboring regions} \\ 0 & \text{elsewhere,} \end{cases} \quad (\text{B.1})$$

with $i, j \in \mathcal{R}$ and where \mathcal{N}_i is the set of neighbors of region $i \in \mathcal{R}$, not including the region itself.²⁴ Consequently, the matrix \mathbf{S} , as defined in Equation (B.1), is symmetric and the rows and columns sum to zero.

We now calculate the product $\beta_j^T \mathbf{S} \beta_j$. Below we omit the subscript j for notational purposes.

²⁴We define neighboring regions as regions that have a common border.

We obtain:

$$\begin{aligned}\boldsymbol{\beta}^T \mathbf{S} \boldsymbol{\beta} &= \left(\sum_{j=1}^R \beta_j s_{j1} \right) \beta_1 + \left(\sum_{j=1}^R \beta_j s_{j2} \right) \beta_2 + \dots + \left(\sum_{j=1}^R \beta_j s_{jR} \right) \beta_R \\ &= \left(|\mathcal{N}_1| \beta_1 - \sum_{j \in \mathcal{N}_1} \beta_j \right) \beta_1 + \left(|\mathcal{N}_2| \beta_2 - \sum_{j \in \mathcal{N}_2} \beta_j \right) \beta_2 + \dots + \left(|\mathcal{N}_R| \beta_R - \sum_{j \in \mathcal{N}_R} \beta_j \right) \beta_R.\end{aligned}$$

If we rewrite the terms in brackets, we obtain:

$$\boldsymbol{\beta}^T \mathbf{S} \boldsymbol{\beta} = \sum_{j \in \mathcal{N}_1} (\beta_1 - \beta_j) \beta_1 + \sum_{j \in \mathcal{N}_1} (\beta_2 - \beta_j) \beta_2 + \dots + \sum_{j \in \mathcal{N}_R} (\beta_R - \beta_j) \beta_R.$$

Next we group the terms containing β_1 , β_2 , etc., and we rewrite this to:

$$\begin{aligned}\boldsymbol{\beta}^T \mathbf{S} \boldsymbol{\beta} &= \sum_{j \in \mathcal{N}_1} (\beta_1 - \beta_j) \beta_1 + \sum_{j \in \mathcal{N}_1} (\beta_j - \beta_1) \beta_j + \sum_{j \in \mathcal{N}_2 \setminus \{1\}} (\beta_2 - \beta_j) \beta_2 + \sum_{j \in \mathcal{N}_2 \setminus \{1\}} (\beta_j - \beta_2) \beta_j + \dots + \\ &\quad \sum_{j \in \mathcal{N}_{R-1} \setminus \{1, \dots, R-2\}} (\beta_{R-1} - \beta_j) \beta_{R-1} + \sum_{j \in \mathcal{N}_{R-1} \setminus \{1, \dots, R-2\}} (\beta_j - \beta_{R-1}) \beta_j,\end{aligned}$$

where, e.g., $\mathcal{N}_k \setminus \{1, \dots, k-1\}$ represents the set of neighbors of region k , excluding the first $k-1$ regions, for $k = 1, 2, \dots, R-1$. After simplifying, we obtain:

$$\boldsymbol{\beta}^T \mathbf{S} \boldsymbol{\beta} = \sum_{j \in \mathcal{N}_1} (\beta_1 - \beta_j)^2 + \sum_{j \in \mathcal{N}_2 \setminus \{1\}} (\beta_2 - \beta_j)^2 + \dots + \sum_{j \in \mathcal{N}_{R-1} \setminus \{1, \dots, R-2\}} (\beta_{R-1} - \beta_j)^2.$$

We conclude that the imposed penalty matrix penalizes the sum of the squared differences between the parameters of neighboring regions.

A toy example is shown in Figure B.1 and Table B.1, where we focus on five NUTS 3 regions in Spain and specify the corresponding quadratic penalty matrix \mathbf{S} .

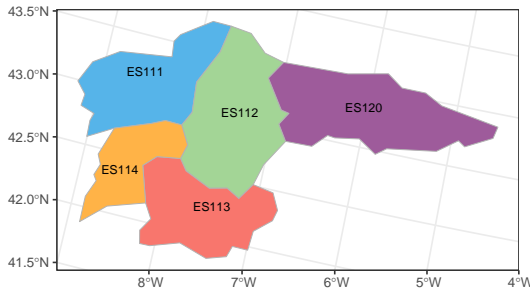


Figure B.1: Five NUTS 3 regions in Spain.

	ES111	ES112	ES113	ES114	ES120
ES111	2	-1	0	-1	0
ES112	-1	4	-1	-1	-1
ES113	0	-1	2	-1	0
ES114	-1	-1	-1	3	0
ES120	0	-1	0	0	1

Table B.1: Quadratic penalty matrix \mathbf{S} .

C Feature engineering

C.1 Construction of population weights

In this appendix, we elaborate on the methodology for calculating the weights used in the weighted aggregation process of a feature to the NUTS 3 geographical level, as described in

Equation (5.2). We follow the notation and concepts introduced in Section 5.1.2. Similarly to Equation (5.1), we define the set of (long,lat) coordinates of the grid $\mathcal{G}^{(2)}$ that fall within the boundaries of a NUTS 3 region $r \in \mathcal{R}$ as:

$$\mathcal{I}_2(r) = \left\{ (\text{long}, \text{lat}) \mid (\text{long}, \text{lat}) \in \mathcal{G}^{(2)} \text{ and } m_{\mathcal{G}^{(2)}}(\text{long}, \text{lat}) = r \right\}.$$

Next, we appoint each longitude-latitude coordinate in the population grid restricted to region r , i.e., $\mathcal{I}_2(r)$, to its closest longitude-latitude coordinate in the feature grid restricted to region r , i.e., $\mathcal{I}_1(r)$. Hereto, we define, for any $(\text{long}, \text{lat}) \in \mathcal{I}_1(r)$, the set:

$$\mathcal{P}^{(\text{long}, \text{lat})}(r) = \left\{ (a, b) \in \mathcal{I}_2(r) \mid d_2((a, b), (\text{long}, \text{lat})) \leq d_2((a, b), (l_1, l_2)) \quad \forall (l_1, l_2) \in \mathcal{I}_1^{(r)} \right\},$$

where d_2 refers to the 2-norm or Euclidean distance. We then calculate the population weights at grid points $(\text{long}, \text{lat}) \in \mathcal{I}_1(r)$ as:

$$\omega_{(\text{long}, \text{lat})} = \frac{\sum_{(a,b) \in \mathcal{P}^{(\text{long}, \text{lat})}(r)} P^{(a,b)}}{\sum_{(a,b) \in \mathcal{I}_2(r)} P^{(a,b)}}, \quad (\text{C.1})$$

where $P^{(a,b)}$ refers to the population count at any grid point (a, b) in the population grid $\mathcal{G}^{(2)}$. The nominator in Equation (C.1) equals the population count attributed to the grid point $(\text{long}, \text{lat})$ of the feature grid and the denominator equals the total population count in the entire NUTS 3 region r . By construction, the sum of the weights in each region r equals one. Figure C.1 illustrates the steps to calculate the population weights in Equation (5.2).

In the scenario where a specific, very small NUTS 3 region $r \in \mathcal{R}$ contains no grid points from the feature grid $\mathcal{G}^{(1)}$, i.e., when $\mathcal{I}_1(r) = \emptyset$, we determine the feature value $\tilde{x}_{t,m,d}^{(r)}$ as the value $\tilde{x}_{t,m,d}^{(\text{long}, \text{lat})}$ at the closest longitude-latitude coordinates from the feature grid to the boundaries of that region.

D XGBoost: algorithm, parameter tuning, and interpretation tools

D.1 Algorithm

For notational purposes, we denote $\mathbf{x}_{t,w}^{(r)}$ as the input vector for the XGBoost model. This vector consists of the (one-week lagged) environmental anomalies, the (one-week lagged) extreme environmental indices, and the region and season-specific covariates, as detailed in Section 5.2.2. Given that we assume a Poisson distribution for the random variable $D_{t,w}^{(r)}$, representing the number of deaths in week $w \in \mathcal{W}_t$ of year $t \in \mathcal{T}$ and in $r \in \mathcal{R}$, we construct the XGBoost model on a logarithmic scale to ensure non-negativity of the outcome values. Hereto, we introduce the function:

$$\mathfrak{f} : \mathcal{R}^q \rightarrow \mathcal{R} : \mathbf{x} \mapsto \log f(\mathbf{x}),$$

where q is the dimension of the input vector $\mathbf{x}_{t,w}^{(r)}$. Algorithm 1 sketches the XGBoost algorithm in pseudo-code (Chen & Guestrin, 2016), where we consider the negative log-likelihood from

ITC31: Imperia

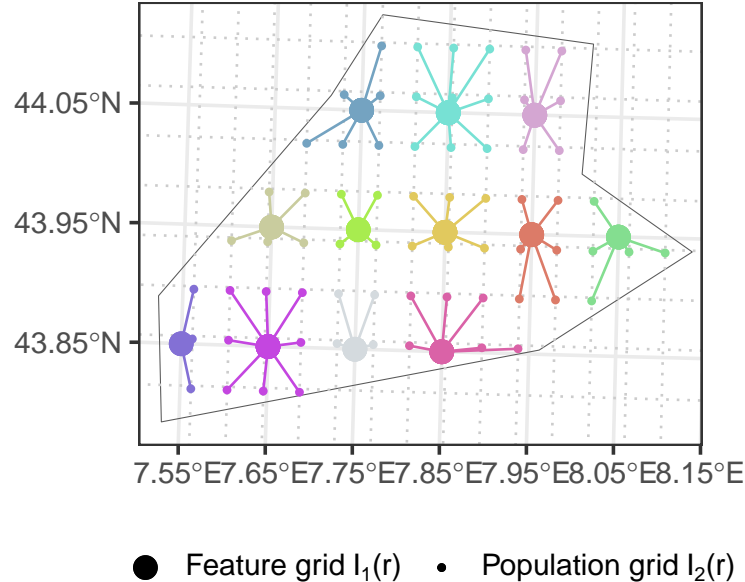


Figure C.1: Visualisation of the calculation of the population weights at each longitude-latitude coordinate of the feature grid (big dots) in the NUTS 3 region Imperia (Northern Italy). We attribute the population count at each population grid point (small dots) to the closest feature grid point (big dots). The solid, light-grey lines represent the feature grid $\mathcal{G}^{(1)}$, while the dotted, light-grey lines represent the population grid $\mathcal{G}^{(2)}$.

Equation (4.5) as the loss function. Since the predictions are constructed on logarithmic scale, the final outcomes of the XGBoost algorithm are:

$$\hat{f}_{\text{XGBoost}}(\mathbf{x}_{t,w}^{(r)}) = \exp(\hat{\mathbf{f}}_{\text{XGBoost}}(\mathbf{x}_{t,w}^{(r)})),$$

for all $t \in \mathcal{T}$, $w \in \mathcal{W}_t$, and $r \in \mathcal{R}$.

The XGBoost algorithm relies on six tuning parameters, detailed in Table D.1. It is important to note that the XGBoost algorithm encompasses a broader set of parameters beyond those explicitly listed in Table 1. The additional parameters, which we classify as hyper-parameters, extend the configurational possibilities of the algorithm. Chen et al. (2019) provide a comprehensive overview of all parameters associated with the XGBoost algorithm.

D.2 Parameter tuning with cross-validation

The T -fold cross-validation process, visualized in Figure D.1, involves training the XGBoost model on $T - 1$ folds and predicting the observations in the remaining hold-out fold, considering various parameter combinations from a predefined tuning grid. This cycle is repeated T times, as illustrated in Figure D.1. Subsequently, for each parameter combination in the tuning grid, the Poisson loss, see Equation (4.5), is computed on the predictions made for the hold-out fold. The average of these loss values across the T different hold-out folds is calculated for each parameter combination. The optimal values for the tuning parameters correspond to the parameter combination that yields the smallest average loss value.

²⁵We select a random subset of `subsample` \times 100% of the training instances and `colsample_bytree` \times 100% of the features.

Algorithm 1: XGBoost algorithm for Poisson distributed outcomes.

Input: the training data $\left\{ \left(\mathbf{x}_{t,w}^{(r)}, \hat{b}_{t,w}^{(r)}, d_{t,w}^{(r)} \right) \right\}_{r \in \mathcal{R}, t \in \mathcal{T}, w \in \mathcal{W}_t}$

Set initial model predictions: $\hat{f}_{(0)}(\mathbf{x}_{t,w}^{(r)}) = 0$ for all $r \in \mathcal{R}$, $t \in \mathcal{T}$ and $w \in \mathcal{W}_t$.

for n **in** $1 : nrounds$ **do**

Calculate the gradient and hessian of the loss function \mathcal{L} :

$$\hat{g}_{(n)}(\mathbf{x}_{t,w}^{(r)}) = \left[\frac{\partial \mathcal{L}(d_{t,w}^{(r)}, f(\mathbf{x}_{t,w}^{(r)}))}{\partial f(\mathbf{x}_{t,w}^{(r)})} \right]_{f(\mathbf{x}_{t,w}^{(r)})=\hat{f}_{(n-1)}(\mathbf{x}_{t,w}^{(r)})} = \hat{b}_{t,w}^{(r)} \cdot e^{\hat{f}_{(n-1)}(\mathbf{x}_{t,w}^{(r)})} - d_{t,w}^{(r)}$$

$$\hat{h}_{(n)}(\mathbf{x}_{t,w}^{(r)}) = \left[\frac{\partial^2 \mathcal{L}(d_{t,w}^{(r)}, f(\mathbf{x}_{t,w}^{(r)}))}{\partial f(\mathbf{x}_{t,w}^{(r)})^2} \right]_{f(\mathbf{x}_{t,w}^{(r)})=\hat{f}_{(n-1)}(\mathbf{x}_{t,w}^{(r)})} = \hat{b}_{t,w}^{(r)} \cdot e^{\hat{f}_{(n-1)}(\mathbf{x}_{t,w}^{(r)})}.$$

Fit a single regression tree $\delta_{(n)}$ of maximum depth `max_depth` and of minimum child weight `min_child_weight` on the training data $(\mathbf{x}_{t,w}^{(r)}, \hat{b}_{t,w}^{(r)}, -\hat{g}_{(n)}(\mathbf{x}_{t,w}^{(r)})/\hat{h}_{(n)}(\mathbf{x}_{t,w}^{(r)}))$:²⁵

$$\hat{\delta}_{(n)} = \arg \min_{\delta \in \Delta} \sum_{r \in \mathcal{R}} \sum_{t \in \mathcal{T}} \sum_{w \in \mathcal{W}_t} \frac{1}{2} \hat{h}_{(n)}(\mathbf{x}_{t,w}^{(r)}) \left[\delta(\mathbf{x}_{t,w}^{(r)}) - \frac{\hat{g}_{(n)}(\mathbf{x}_{t,w}^{(r)})}{\hat{h}_{(n)}(\mathbf{x}_{t,w}^{(r)})} \right]^2.$$

Update the model predictions with learning rate `eta`:

$$\hat{f}_{(n)}(\mathbf{x}_{t,w}^{(r)}) = \hat{f}_{(n-1)}(\mathbf{x}_{t,w}^{(r)}) + \text{eta} \cdot \hat{\delta}_{(n)}(\mathbf{x}_{t,w}^{(r)}).$$

end

Output: $\hat{f}_{\text{XGBoost}}(\mathbf{x}_{t,w}^{(r)}) = \hat{f}_{(nrounds)}(\mathbf{x}_{t,w}^{(r)})$ for all $r \in \mathcal{R}$, $t \in \mathcal{T}$ and $w \in \mathcal{W}_t$.

Tuning parameter	Explanation
<code>nrounds</code>	The maximum number of boosting iterations.
<code>eta</code>	Learning rate: adjusts the impact of each tree by multiplying it with a factor <code>eta</code> when incorporating it into the current approximation.
<code>max_depth</code>	The maximum depth of a tree.
<code>subsample</code>	Subsample ratio of the training data. A value of, e.g., 0.75, means that the algorithm randomly selects 75% of the training observations each time it constructs a tree.
<code>colsample_bytree</code>	Subsample ratio of the columns or features when constructing trees.
<code>min_child_weight</code>	Minimum sum of observation weights, i.e. hessian values, required in each node of a tree.

Table D.1: Tuning parameters in the XGBoost algorithm.

D.3 Interpretation tools

Feature importance Following the notation from Section 4.2, we let $\Delta \mathcal{L}_n(X_l)$ be the total reduction in the Poisson loss function, see Equation (4.5), caused by splits associated to feature

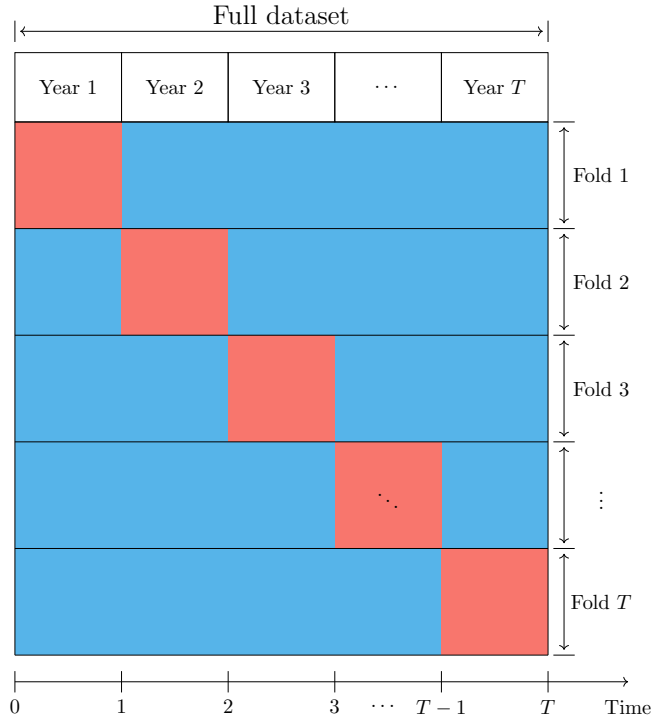


Figure D.1: Visualisation of the proposed T -fold cross-validation for tuning the parameters in the XGBoost model. The blue boxes refer to the training folds and the red boxes to the validation folds in each split.

X_l in the tree built during iteration n of the XGBoost algorithm. We then calculate the (unscaled) feature importance of the feature X_l as:

$$\mathcal{V}_{\text{imp}}(X_l) = \frac{1}{\text{nrounds}} \sum_{n=1}^{\text{nrounds}} \Delta \mathcal{L}_n(X_l),$$

where we normalize the obtained importance measure to ensure interpretability and comparability. As a result, the sum of the feature importances for all features adds up to one.

Accumulated Local Effects The ALE effect of a feature X_l at value x is defined as:

$$f_{l,\text{ALE}}(x) = \int_{z_{0,l}}^x \mathbb{E} \left[\frac{\partial f(X_1, X_2, \dots, X_p)}{\partial X_l} \middle| X_l = z_l \right] dz_l - c_l \quad (\text{D.1})$$

where $z_{0,l}$ is a lower bound on the range of X_l , typically chosen as the minimum value observed in the data. We interpret the integrand in Equation (D.1) as the expected change in the prediction function $f(\cdot)$ when slightly changing the feature X_l around the value z_l , also known as the local effect. Afterwards we accumulate these local effects by integrating them from $z_{0,l}$ to x to unravel the global effect of the feature X_l on the response. Taking the conditional expectation in Equation (D.1) isolates the effect of the feature X_l on the prediction function $f(\cdot)$ from the effects of all other, (possibly) correlated features. Further, [Apley and Zhu \(2020\)](#) introduce the constant c_l such that the expectation of the random variable $f_{l,\text{ALE}}(X_l)$ equals zero.

To investigate interaction effects between two environmental features, say X_k and X_l , we calculate the ALE interaction effect ([Apley & Zhu, 2020](#)). Let $z_{0,k}$ and $z_{0,l}$ be the lower bounds

on the ranges of X_k and X_l respectively, then:

$$f_{k,l,\text{ALE}}(x, y) = \int_{z_{0,k}}^x \int_{z_{0,l}}^y \mathbb{E} \left[\frac{\partial^2 f(X_1, X_2, \dots, X_p)}{\partial X_l \partial X_k} \middle| X_k = z_k, X_l = z_l \right] dz_l dz_k - c_{k,l}, \quad (\text{D.2})$$

where now the conditional expectation is taken with respect to the joint distribution of the random variables X_j for $j \neq k, l$. Equation (D.2) considers the second order partial effects and accumulates these effects in two dimensions. As such, the main effects of the features are not considered in the calculation and the ALE interaction effect should therefore be interpreted as an additional interaction effect on top of the main effects. Further, the constant $c_{k,l}$ is determined such that the expectation of $f_{k,l,\text{ALE}}(X_k, X_l)$ equals zero. Appendix D.3 outlines the estimation procedure for calculating the ALE (interaction) effect on the training data.

Since we do not have a closed-form expression for the prediction function f of the fitted XGBoost model, the expressions of the ALE (interaction) effects in Equations (D.1) and (D.2) can not be calculated analytically. Therefore, we estimate these ALE effects using the training data represented in Equation (4.6). We explain the procedure for estimating the ALE effect of a single feature X_l .

We consider the feature space of the random variable X_l in the training data and divide it into K non-overlapping bins, i.e., $z_{0,l} < z_{1,l} < \dots < z_{K,l}$, where $z_{0,l}$ and $z_{K,l}$ are the covariate's observed minimum and maximum value respectively. Further, let $\mathfrak{X}_l(k)$ represent the set of training instances for which the l -th feature value falls into the k -th bin, i.e.,

$$\mathfrak{X}_l(k) = \left\{ \mathbf{x}_{t,w}^{(r)} \mid z_{k-1} < x_{l,t,w}^{(r)} < z_k \right\},$$

with $k \in \{1, 2, \dots, K\}$. We denote $n_l(k) = |\mathfrak{X}_l(k)|$ for the number of training instances that fall into the k -th bin. Now consider any x in the feature space of X_l and let $k_l(x)$ be the number of the bin the value x belongs to. Next, we approximate the partial order derivative in Equation (D.1) with a first-order finite difference and obtain (Molnar, 2019):

$$\tilde{f}_{l,\text{ALE}}(x) = \sum_{k=1}^{k_l(x)} \frac{1}{n_l(k)} \sum_{\mathbf{x}_{t,w}^{(r)} \in \mathfrak{X}_l(k)} \left[f(z_{k,l}, \mathbf{x}_{-l,t,w}^{(r)}) - f(z_{k-1,l}, \mathbf{x}_{-l,t,w}^{(r)}) \right]$$

where $\mathbf{x}_{-l,t,w}^{(r)}$ is the feature vector where the l -th feature value has been removed from. The centred ALE effect then equals:

$$\hat{f}_{l,\text{ALE}}(x) = \tilde{f}_{l,\text{ALE}}(x) - \frac{1}{n} \sum_{r \in \mathcal{R}} \sum_{t \in \mathcal{T}} \sum_{w \in \mathcal{W}} \tilde{f}_{l,\text{ALE}}(x_{l,t,w}^{(r)}), \quad (\text{D.3})$$

with n the number of training instances. We estimate the ALE interaction effects from Equation (D.2) in a similar way. However, instead of considering one-dimensional bins, we now need to consider rectangular grid cells. Furthermore, we approximate the second-order partial derivative by a second-order finite difference, see Apley and Zhu (2020) and Molnar (2019) for further details.

D.4 Statistical in-sample tests

Weekly, region-specific observations We perform a statistical in-sample test to investigate the benefit of incorporating environmental factors into the weekly mortality model. Hereto, we

compare the difference in the in-sample Poisson deviance between the XGBoost model and the baseline model. We calculate the Poisson deviance of the XGBoost model as:

$$\text{POI_Dev} = 2 \sum_{r \in \mathcal{R}} \sum_{t \in \mathcal{T}} \sum_{w \in \mathcal{W}_t} \left(d_{t,w}^{(r)} \cdot \log \frac{d_{t,w}^{(r)}}{\hat{d}_{t,w}^{(r)}} - \left(d_{t,w}^{(r)} - \hat{d}_{t,w}^{(r)} \right) \right), \quad (\text{D.4})$$

where $\hat{d}_{t,w}^{(r)}$ represents the estimated number of deaths by the XGBoost model. We compute the Poisson deviance of the baseline model in a similar way, but replace the estimated number of deaths $\hat{d}_{t,w}^{(r)}$ by the estimated baseline number of deaths $\hat{b}_{t,w}^{(r)}$. In a global analysis across all NUTS 3 regions, the Poisson deviance on the entire training dataset is 252 912.3 when calculated with the baseline model and 220 766.0 when calculated with the XGBoost model, representing a reduction of 12.71%.

Additionally, we conduct a similar analysis on a regional basis by comparing the in-sample Poisson deviance on the training datasets restricted to each region, calculated with both the baseline and XGBoost model. Figure D.2 shows the relative change in these Poisson deviances in each region with respect to the baseline model. We observe that the most significant change in the Poisson deviance is observed in the southern regions, indicating a substantial improvement when incorporating weather and air pollution factors into the weekly baseline mortality model. Conversely, in the northern regions, the added value of such incorporation appears to be limited.

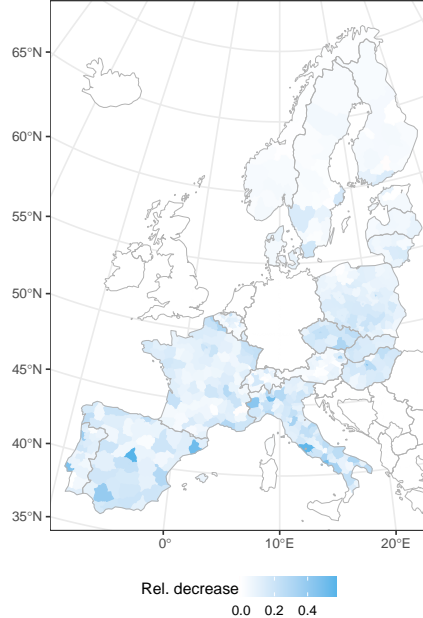


Figure D.2: The relative change in the Poisson deviance of the XGBoost model, incorporating weather and air pollution factors, and the baseline model in each NUTS 3 region.

Temporally aggregated observations We evaluate the in-sample Poisson deviance in each region for the Poisson GLM in Equation (5.6), the weekly Serfling-type baseline model in Equation (3.1), and the machine learning model in Equation (3.4). Figure D.3a visualizes the preferred model in each region, i.e., the model which leads to the lowest in-sample Poisson deviance. We find that approximately 80% of the regions favour the XGBoost model. However, in the

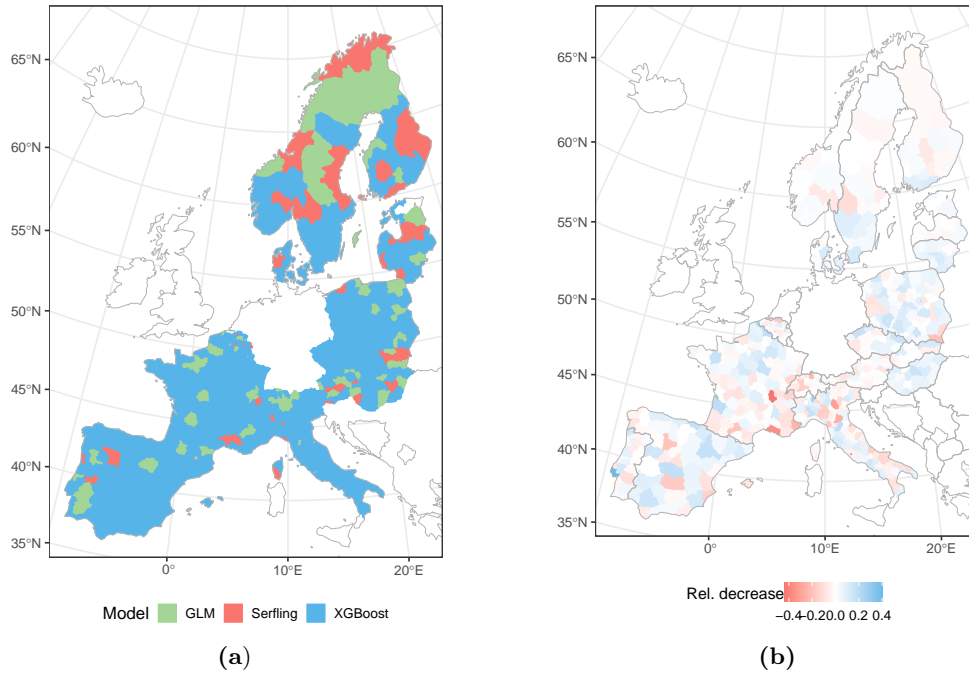


Figure D.3: Panel (a) displays an overview of the model with the lowest Poisson deviance in the NUTS 3 European regions. Panel (b) shows the relative change in the Poisson deviance of the deaths estimated by the XGBoost model, integrating environmental features, relative to the Poisson deviance estimated by the weekly baseline model, in each NUTS 3 region for the year 2019.

northern regions, the Poisson GLM estimated on annual mortality statistics is often the preferred model. One potential reason is the low population exposure and the, consequently, fewer deaths in these regions, making the added value of environmental features limited in these regions.

D.5 Statistical out-of-sample test

We evaluate the out-of-sample Poisson deviance in each region for the year 2019 using both the weekly mortality baseline model and the XGBoost model incorporating environmental factors, see Section 5.5. Figure D.3b illustrates the relative change in the Poisson deviance of the deaths estimated by the XGBoost model relative to the deaths estimated by the weekly baseline model, defined as:

$$\frac{\text{POI}_\text{Dev}_b - \text{POI}_\text{DevXGB}}{\text{POI}_\text{Dev}_b},$$

where POI_Dev_b and POI_DevXGB are the Poisson deviances calculated using the deaths obtained from the estimated weekly baseline and XGBoost model, respectively, see Equation (D.4). A positive value for the above defined criterion indicates an improvement of the XGBoost model with respect to the baseline model.

References

- Alberdi, J. C., Díaz, J., Montero, J. C., & Mirón, I. (1998). Daily mortality in Madrid

- community 1986–1992: Relationship with meteorological variables. *European Journal of Epidemiology*, 14(6), 571–578.
- Almon, S. (1965). The distributed lag between capital appropriations and expenditures. *Econometrica: Journal of the Econometric Society*, 33(1), 178–196. doi: [10.2307/1911894](https://doi.org/10.2307/1911894)
- American Academy of Actuaries, Casualty Actuarial Society, Canadian Institute of Actuaries, & Society of Actuaries. (2016). *Actuaries Climate Index*. <https://actuariesclimateindex.org>. (Accessed 05-02-2024)
- Anderson, B. G., & Bell, M. L. (2009). Weather-related mortality: how heat, cold, and heat waves affect mortality in the United States. *Epidemiology*, 20(2), 205–213. doi: [10.1097/EDE.0b013e318190ee08](https://doi.org/10.1097/EDE.0b013e318190ee08)
- Apley, D. W., & Zhu, J. (2020). Visualizing the effects of predictor variables in black box supervised learning models. *Journal of the Royal Statistical Society Series B: Statistical Methodology*, 82(4), 1059–1086. doi: [10.1111/rssb.12377](https://doi.org/10.1111/rssb.12377)
- Armstrong, B. (2006). Models for the relationship between ambient temperature and daily mortality. *Epidemiology*, 17(6), 624–631. doi: [10.1097/01.ede.0000239732.50999.8f](https://doi.org/10.1097/01.ede.0000239732.50999.8f)
- Balakrishnan, K., Dey, S., Gupta, T., Dhaliwal, R., Brauer, M., Cohen, A. J., ... Dandona, L. (2019). The impact of air pollution on deaths, disease burden, and life expectancy across the states of India: The Global Burden of Disease Study 2017. *The Lancet Planetary Health*, 3(1), e26–e39. doi: [10.1016/S2542-5196\(18\)30261-4](https://doi.org/10.1016/S2542-5196(18)30261-4)
- Ballester, J., Quijal-Zamorano, M., Méndez Turrubiates, R. F., Pegenaute, F., Herrmann, F. R., Robine, J. M., ... Achebak, H. (2023). Heat-related mortality in europe during the summer of 2022. *Nature medicine*, 29(7), 1857–1866. doi: [10.1038/s41591-023-02649-1](https://doi.org/10.1038/s41591-023-02649-1)
- Barnett, A. (2010). What measure of temperature is the best predictor of mortality? *Environmental Research*, 110(6), 604–611. doi: [10.1097/01.ede.0000362214.90491.53](https://doi.org/10.1097/01.ede.0000362214.90491.53)
- Basu, R., & Samet, J. M. (2002). Relation between elevated ambient temperature and mortality: A review of the epidemiologic evidence. *Epidemiologic Reviews*, 24(2), 190–202. doi: [10.1093/epirev/mxf007](https://doi.org/10.1093/epirev/mxf007)
- Bentayeb, M., Wagner, V., Stempfelet, M., Zins, M., Goldberg, M., Pascal, M., ... Lefranc, A. (2015). Association between long-term exposure to air pollution and mortality in france: A 25-year follow-up study. *Environment International*, 85, 5–14. doi: [10.1016/j.envint.2015.08.006](https://doi.org/10.1016/j.envint.2015.08.006)
- Bergmeir, C., Hyndman, R. J., & Koo, B. (2018). A note on the validity of cross-validation for evaluating autoregressive time series prediction. *Computational Statistics & Data Analysis*, 120, 70–83. doi: [10.1016/j.csda.2017.11.003](https://doi.org/10.1016/j.csda.2017.11.003)
- Booth, H., & Tickle, L. (2008). Mortality modelling and forecasting: A review of methods. *Annals of actuarial science*, 3(1-2), 3–43. doi: [10.1017/S1748499500000440](https://doi.org/10.1017/S1748499500000440)
- Braga, A. L. F., Zanobetti, A., & Schwartz, J. (2001). The time course of weather-related deaths. *Epidemiology*, 12(6), 662–667. doi: [10.1097/00001648-200111000-00014](https://doi.org/10.1097/00001648-200111000-00014)
- Braga, A. L. F., Zanobetti, A., & Schwartz, J. (2002). The effect of weather on respiratory and cardiovascular deaths in 12 US cities. *Environmental Health Perspectives*, 110(9), 859–863. doi: [10.1289/ehp.02110859](https://doi.org/10.1289/ehp.02110859)
- Breiman, L., & Ihaka, R. (1984). Nonlinear discriminant analysis via scaling and ACE. Department of Statistics, University of California.
- Brunekreef, B., & Holgate, S. T. (2002). Air pollution and health. *The Lancet*, 360(9341), 1233–1242. doi: [10.1016/S0140-6736\(02\)11274-8](https://doi.org/10.1016/S0140-6736(02)11274-8)
- Cairns, A. J., Kallestrup-Lamb, M., Rosenskjold, C., Blake, D., & Dowd, K. (2019). Modelling socio-economic differences in mortality using a new affluence index. *ASTIN Bulletin*, 49(3), 555–590. doi: [10.1017/asb.2019.14](https://doi.org/10.1017/asb.2019.14)
- Carleton, T., Jina, A., Delgado, M., Greenstone, M., Houser, T., Hsiang, S., ... Zhang, A. T.

- (2022). Valuing the global mortality consequences of climate change accounting for adaptation costs and benefits*. *The Quarterly Journal of Economics*, 137(4), 2037–2105. doi: [10.1093/qje/qjac020](https://doi.org/10.1093/qje/qjac020)
- Center for International Earth Science Information Network – CIESIN – Columbia University.
- (2018). *Gridded population of the world, version 4 (GPWv4): Population count, revision 11*. Palisades, New York: NASA Socioeconomic Data and Applications Center (SEDAC). (Accessed 01-08-2023) doi: [10.7927/H4JW8BX5](https://doi.org/10.7927/H4JW8BX5)
- Chen, T., & Guestrin, C. (2016). XGBoost: A scalable tree boosting system. In *Proceedings of the 22nd ACM SIGKDD International Conference on Knowledge Discovery and Data Mining* (pp. 785–794). doi: [10.1145/2939672.2939785](https://doi.org/10.1145/2939672.2939785)
- Chen, T., He, T., Benesty, M., & Khotilovich, V. (2019). Package ‘xgboost’. *R version*, 90, 1–66.
- Copernicus Climate Change Service, Climate Data Store. (2020). *E-OBS daily gridded meteorological data for Europe from 1950 to present derived from in-situ observations*. Copernicus Climate Change Service (C3S) Climate Data Store (CDS). (Accessed 01-09-2023) doi: [10.24381/cds.151d3ec6](https://doi.org/10.24381/cds.151d3ec6)
- de Schrijver, E., Folly, C. L., Schneider, R., Royé, D., Franco, O. H., Gasparini, A., & Vicedo-Cabrera, A. M. (2021). A comparative analysis of the temperature-mortality risks using different weather datasets across heterogeneous regions. *GeoHealth*, 5(5). doi: [10.1029/2020GH000363](https://doi.org/10.1029/2020GH000363)
- Devalia, J. L., Rusznak, C., Herdman, M. J., Trigg, C. J., Davies, R. J., & Tarraf, H. (1994). Effect of nitrogen dioxide and sulphur dioxide on airway response of mild asthmatic patients to allergen inhalation. *The Lancet*, 344(8938), 1668–1671. doi: [10.1016/S0140-6736\(94\)90458-8](https://doi.org/10.1016/S0140-6736(94)90458-8)
- DiCiccio, T. J., & Efron, B. (1996). Bootstrap confidence intervals. *Statistical science*, 11(3), 189–228. doi: [10.1214/ss/1032280214](https://doi.org/10.1214/ss/1032280214)
- Dong, M., Bruhn, A., Shang, H. L., & Hui, F. (2024). Assessing the impact of climate risk stresses on life insurance portfolios. *Asia-Pacific Journal of Risk and Insurance*, 18(1), 87–114. doi: [10.1515/apjri-2023-0010](https://doi.org/10.1515/apjri-2023-0010)
- Dong, Z. M., Shang, H. L., & Bruhn, A. (2022). Air pollution and mortality impacts. *Risks*, 10(6), 126. doi: [10.3390/risks10060126](https://doi.org/10.3390/risks10060126)
- EIOPA. (2021). *Opinion on the supervision of the use of climate change risk scenarios in ORSA*. European Insurance and Occupations Pensions Authority (EIOPA) Frankfurt. (Accessed 1-03-2024)
- Enchev, V., Kleinow, T., & Cairns, A. J. (2017). Multi-population mortality models: fitting, forecasting and comparisons. *Scandinavian Actuarial Journal*, 2017(4), 319–342. doi: [10.1080/03461238.2015.1133450](https://doi.org/10.1080/03461238.2015.1133450)
- Fischer, E. M., & Knutti, R. (2013). Robust projections of combined humidity and temperature extremes. *Nature Climate Change*, 3(2), 126–130. doi: [10.1038/nclimate1682](https://doi.org/10.1038/nclimate1682)
- Friedman, J. H. (2001). Greedy function approximation: A gradient boosting machine. *Annals of Statistics*, 29(5), 1189–1232. doi: [10.1214/aos/1013203451](https://doi.org/10.1214/aos/1013203451)
- Gasparini, A., & Armstrong, B. (2011). The impact of heat waves on mortality. *Epidemiology*, 22(1), 68. doi: [10.1097/EDE.0b013e3181fdcd99](https://doi.org/10.1097/EDE.0b013e3181fdcd99)
- Gasparini, A., & Armstrong, B. (2013). Reducing and meta-analysing estimates from distributed lag non-linear models. *BMC Medical Research Methodology*, 13(1), 1–10. doi: [10.1186/1471-2288-13-1](https://doi.org/10.1186/1471-2288-13-1)
- Gasparini, A., Armstrong, B., & Kenward, M. G. (2010). Distributed lag non-linear models. *Statistics in Medicine*, 29(21), 2224–2234. doi: [10.1002/sim.3940](https://doi.org/10.1002/sim.3940)
- Gasparini, A., Armstrong, B., & Kenward, M. G. (2012). Multivariate meta-analysis for non-

- linear and other multi-parameter associations. *Statistics in Medicine*, 31(29), 3821–3839. doi: [10.1002/sim.5471](https://doi.org/10.1002/sim.5471)
- Gasparrini, A., Guo, Y., Hashizume, M., Lavigne, E., Zanobetti, A., Schwartz, J., ... Armstrong, B. (2015). Mortality risk attributable to high and low ambient temperature: A multicountry observational study. *The Lancet*, 386(9991), 369–375. doi: [10.1016/S0140-6736\(14\)62114-0](https://doi.org/10.1016/S0140-6736(14)62114-0)
- Gasparrini, A., & Leone, M. (2014). Attributable risk from distributed lag models. *BMC Medical Research Methodology*, 14(1), 1–8. doi: [10.1186/1471-2288-14-55](https://doi.org/10.1186/1471-2288-14-55)
- Gervini, D., & Yohai, V. J. (2002). A class of robust and fully efficient regression estimators. *The Annals of Statistics*, 30(2), 583–616. doi: [10.1214/aos/1021379866](https://doi.org/10.1214/aos/1021379866)
- Guo, Y., Gasparrini, A., Armstrong, B. G., Tawatsupa, B., Tobias, A., Lavigne, E., ... Tong, S. (2017). Heat wave and mortality: A multicountry, multicomunity study. *Environmental Health Perspectives*, 125(8), 087006. doi: [10.1289/EHP1026](https://doi.org/10.1289/EHP1026)
- Hajat, S., Armstrong, B., Baccini, M., Biggeri, A., Bisanti, L., Russo, A., ... Kosatsky, T. (2006). Impact of high temperatures on mortality: is there an added heat wave effect? *Epidemiology*, 17(6), 632–638. doi: [10.1097/01.ede.0000239688.70829.63](https://doi.org/10.1097/01.ede.0000239688.70829.63)
- Hastie, T., Tibshirani, R., & Friedman, J. (2001). *The elements of statistical learning*. Springer New York, NY. doi: [10.1007/978-0-387-84858-7](https://doi.org/10.1007/978-0-387-84858-7)
- Hoek, G., Krishnan, R. M., Beelen, R., Peters, A., Ostro, B., Brunekreef, B., & Kaufman, J. D. (2013). Long-term air pollution exposure and cardio-respiratory mortality: a review. *Environmental health*, 12, 1–16. doi: [10.1186/1476-069X-12-43](https://doi.org/10.1186/1476-069X-12-43)
- Hulme, M., & Jenkins, G. (1998). *Climate change scenarios for the United Kingdom – Technical report No 1* (Publisher's version ed.; Tech. Rep.).
- Institut national de l'environnement industriel et des risques (Ineris), Aarhus University, Norwegian Meteorological Institute (MET Norway), Jülich Institut für Energie- und Klimaforschung (IEK), Institute of Environmental Protection – National Research Institute (IEP-NRI), Koninklijk Nederlands Meteorologisch Instituut (KNMI), ... Barcelona Supercomputing Center (BSC) (2022). *CAMS European air quality forecasts, ENSEMBLE data*. <https://ads.atmosphere.copernicus.eu/cdsapp#!/dataset/cams-europe-air-quality-reanalyses?tab=overview>. Copernicus Atmosphere Monitoring Service (CAMS) Atmosphere Data Store (ADS). (Accessed 01-08-2023)
- Jdanov, D. A., Galarza, A. A., Shkolnikov, V. M., Jaslionis, D., Németh, L., Leon, D. A., ... Barbieri, M. (2021). The short-term mortality fluctuation data series, monitoring mortality shocks across time and space. *Scientific Data*, 8(1), 235. doi: [10.1038/s41597-021-01019-1](https://doi.org/10.1038/s41597-021-01019-1)
- Keatinge, W. R., Donaldson, G. C., Cordioli, E., Martinelli, M., Kunst, A. E., Mackenbach, J. P., ... Vuori, I. (2000). Heat related mortality in warm and cold regions of Europe: Observational study. *BMJ*, 321(7262), 670–673. doi: [10.1136/bmj.321.7262.670](https://doi.org/10.1136/bmj.321.7262.670)
- Li, H., & Tang, Q. (2022). Joint extremes in temperature and mortality: A bivariate POT approach. *North American Actuarial Journal*, 26(1), 43–63. doi: [10.1080/10920277.2020.1823236](https://doi.org/10.1080/10920277.2020.1823236)
- Li, L., Li, H., & Panagiotelis, A. (2024). Boosting domain-specific models with shrinkage: An application in mortality forecasting. *International Journal of Forecasting*. doi: [10.1016/j.ijforecast.2024.05.001](https://doi.org/10.1016/j.ijforecast.2024.05.001)
- Lovett, A. A., Bentham, C. G., & Flowerdew, R. (1986). Analysing geographic variations in mortality using Poisson regression: The example of ischaemic heart disease in England and Wales 1969–1973. *Social Science & Medicine*, 23(10), 935–943. doi: [10.1016/0277-9536\(86\)90251-0](https://doi.org/10.1016/0277-9536(86)90251-0)
- Meehl, G. A., & Tebaldi, C. (2004). More intense, more frequent, and longer lasting heat waves

- in the 21st century. *Science*, 305(5686), 994–997. doi: [10.1126/science.1098704](https://doi.org/10.1126/science.1098704)
- Molnar, C. (2019). *Interpretable machine learning*. [Online]. Available: <https://christophm.github.io/interpretable-ml-book/>.
- Msemburi, W., Karlinsky, A., Knutson, V., Aleshin-Guendel, S., Chatterji, S., & Wakefield, J. (2023). The WHO estimates of excess mortality associated with the COVID-19 pandemic. *Nature*, 613(7942), 130–137. doi: [10.1038/s41586-022-05522-2](https://doi.org/10.1038/s41586-022-05522-2)
- Mudway, I. S., & Kelly, F. J. (2000). Ozone and the lung: A sensitive issue. *Molecular Aspects of Medicine*, 21, 1–48. doi: [10.1016/s0098-2997\(00\)00003-0](https://doi.org/10.1016/s0098-2997(00)00003-0)
- Nelder, J. A., & Wedderburn, R. W. M. (1972). Generalized linear models. *Journal of the Royal Statistical Society: Series A (General)*, 135(3), 370–384. doi: [10.2307/2344614](https://doi.org/10.2307/2344614)
- Nielsen, J., Krause, T. G., & Mølbak, K. (2018). Influenza-associated mortality determined from all-cause mortality, Denmark 2010/11–2016/17: the FluMOMO model. *Influenza and Other Respiratory Viruses*, 12(5), 591–604. doi: [10.1111/irv.12564](https://doi.org/10.1111/irv.12564)
- Nielsen, J., Vestergaard, L. S., Richter, L., Schmid, D., Bustos, N., Asikainen, T., ... Krause, T. G. (2019). European all-cause excess and influenza-attributable mortality in the 2017/18 season: Should the burden of influenza B be reconsidered? *Clinical Microbiology and Infection*, 25(10), 1266–1276. doi: [10.1016/j.cmi.2019.02.011](https://doi.org/10.1016/j.cmi.2019.02.011)
- Orellano, P., Reynoso, J., Quaranta, N., Bardach, A., & Ciapponi, A. (2020). Short-term exposure to particulate matter (PM10 and PM2.5), nitrogen dioxide (NO₂), and ozone (O₃) and all-cause and cause-specific mortality: Systematic review and meta-analysis. *Environment International*, 142, 105876. doi: [10.1016/j.envint.2020.105876](https://doi.org/10.1016/j.envint.2020.105876)
- Pascal, M., Falq, G., Wagner, V., Chatignoux, E., Corso, M., Blanchard, M., ... Larrieu, S. (2014). Short-term impacts of particulate matter (PM10, PM10–2.5, PM2.5) on mortality in nine French cities. *Atmospheric Environment*, 95, 175–184. doi: [10.1016/j.atmosenv.2014.06.030](https://doi.org/10.1016/j.atmosenv.2014.06.030)
- Pattenden, S., Nikiforov, B., & Armstrong, B. (2003). Mortality and temperature in Sofia and London. *Journal of Epidemiology and Community Health*, 57(8), 628–633. doi: [10.1136/jech.57.8.628](https://doi.org/10.1136/jech.57.8.628)
- Pitacco, E. (2009). *Modelling longevity dynamics for pensions and annuity business*. Oxford University Press.
- Pope, C. A., & Schwartz, J. (1996). Time series for the analysis of pulmonary health data. *American Journal of Respiratory and Critical Care medicine*, 154(6), S229–S233. doi: [10.1164/ajrccm/154.6.Pt_2.S229](https://doi.org/10.1164/ajrccm/154.6.Pt_2.S229)
- Rückerl, R., Schneider, A., Breitner, S., Cyrys, J., & Peters, A. (2011). Health effects of particulate air pollution: A review of epidemiological evidence. *Inhalation Toxicology*, 23(10), 555–592. doi: [10.3109/08958378.2011.593587](https://doi.org/10.3109/08958378.2011.593587)
- Schöley, J. (2021). Robustness and bias of European excess death estimates in 2020 under varying model specifications. *MedRxiv*. doi: [10.1101/2021.06.04.21258353](https://doi.org/10.1101/2021.06.04.21258353)
- Schwartz, J. (2000). The distributed lag between air pollution and daily deaths. *Epidemiology*, 11(3), 320–326. doi: [10.1097/00001648-200005000-00016](https://doi.org/10.1097/00001648-200005000-00016)
- Schwartz, J. (2001). Is there harvesting in the association of airborne particles with daily deaths and hospital admissions? *Epidemiology*, 12(1), 55–61. doi: [10.1097/00001648-200101000-00010](https://doi.org/10.1097/00001648-200101000-00010)
- Serfling, R. E. (1963). Methods for current statistical analysis of excess pneumonia-influenza deaths. *Public Health Reports*, 78(6), 494–506.
- Sunyer, J., Castellsagué, J., Sáez, M., Tobias, A., & Antó, J. M. (1996). Air pollution and mortality in Barcelona. *Journal of Epidemiology & Community Health*, 50(Suppl 1), s76–s80. doi: [10.1136/jech.50.suppl_1.s76](https://doi.org/10.1136/jech.50.suppl_1.s76)
- The Eurowinter Group. (1997). Cold exposure and winter mortality from ischaemic heart

- disease, cerebrovascular disease, respiratory disease, and all causes in warm and cold regions of Europe. *The Lancet*, 349(9062), 1341–1346. doi: [10.1016/S0140-6736\(96\)12338-2](https://doi.org/10.1016/S0140-6736(96)12338-2)
- Verhoeff, A. P., Hoek, G., Schwartz, J., & van Wijnen, J. H. (1996). Air pollution and daily mortality in Amsterdam. *Epidemiology*, 7(3), 225–230. doi: [10.1097/00001648-199605000-00002](https://doi.org/10.1097/00001648-199605000-00002)
- Vestergaard, L. S., Nielsen, J., Richter, L., Schmid, D., Bustos, N., Braeye, T., ... Mølbak, K. (2020). Excess all-cause mortality during the COVID-19 pandemic in Europe – preliminary pooled estimates from the EuroMOMO network, March to April 2020. *Eurosurveillance*, 25(26), 2001214. doi: [10.2807/1560-7917.ES.2020.25.26.2001214](https://doi.org/10.2807/1560-7917.ES.2020.25.26.2001214)
- Villegas, A. M., & Haberman, S. (2014). On the modeling and forecasting of socioeconomic mortality differentials: An application to deprivation and mortality in england. *North American Actuarial Journal*, 18(1), 168–193. doi: [10.1080/10920277.2013.866034](https://doi.org/10.1080/10920277.2013.866034)
- Weilnhammer, V., Schmid, J., Mittermeier, I., Schreiber, F., Jiang, L., Pastuhovic, V., ... Heinze, S. (2021). Extreme weather events in europe and their health consequences—a systematic review. *International Journal of Hygiene and Environmental Health*, 233, 113688. doi: [10.1016/j.ijheh.2021.113688](https://doi.org/10.1016/j.ijheh.2021.113688)
- Wen, J., Cairns, A. J., & Kleinow, T. (2023). Modelling socio-economic mortality at neighbourhood level. *ASTIN Bulletin: The Journal of the IAA*, 53(2), 285–310. doi: [10.1017/asb.2023.12](https://doi.org/10.1017/asb.2023.12)
- Wood, S. N. (2015). Package “mgcv”. *R Package Version*, 1(29), 1–7.
- Wood, S. N. (2017). *Generalized additive models: An introduction with R*. CRC Press. doi: [10.1201/9781315370279](https://doi.org/10.1201/9781315370279)
- Zanobetti, A., Wand, M. P., Schwartz, J., & Ryan, L. M. (2000). Generalized additive distributed lag models: Quantifying mortality displacement. *Biostatistics*, 1(3), 279–292. doi: [10.1093/biostatistics/1.3.279](https://doi.org/10.1093/biostatistics/1.3.279)